

Understanding the Nanoscale Structure of Inverted Hexagonal Phase Lyotropic Liquid Crystal Polymer Membranes

Benjamin J. Coscia,[†] Joseph Yelk,[‡] Matthew A. Glaser,[‡] Douglas L. Gin,^{†,¶}
Xunda Feng,[§] and Michael R. Shirts^{*,†}

[†]*Department of Chemical and Biological Engineering, University of Colorado Boulder,
Boulder, CO 80309, USA*

[‡]*Department of Physics, University of Colorado Boulder, Boulder CO, 80309, USA*

[¶]*Department of Chemistry and Biochemistry, University of Colorado Boulder, Boulder CO
80309, USA*

[§]*Department of Chemical and Environmental Engineering, Yale University, New Haven,
Connecticut 06511, USA*

E-mail: michael.shirts@colorado.edu

Abstract

Periodic, nanostructured porous polymer membranes made from the cross-linked inverted hexagonal phase of self-assembled lyotropic liquid crystals (LLCs) are a promising class of materials for selective separations. In this work, we investigate an experimentally characterized LLC polymer membrane using atomistic molecular modeling. In particular, we compare simulated X-ray diffraction (XRD) patterns with experimental XRD data to quantify and understand the differences between simulation and experiment. We find that the nanopores are likely composed of 5 columns of stacked LLC monomers which surround each hydrophilic core. Evidence suggests that these columns likely move independently of each other over longer time scales than accessible via atomistic simulation. We also find that WAXS structural features previously attributed to monomer tail tilt is likely instead due to ordered tail packing. Although this system has been reported as dry, we show that small amounts of water are necessary to reproduce all features from the experimental XRD pattern due to asymmetries introduced by hydrogen bonds between the monomer head groups and water molecules. Finally, we explore the composition and structure of the nanopores and reveal that there exists a composition gradient rather than an abrupt partition between the hydrophilic and hydrophobic regions. A caveat is that the time scales of the dynamics are extremely long for this system, resulting in simulated structures that appear too ordered, thus requiring careful examination of the metastable states observed in order to draw any conclusions. The clearer picture of the nanoscopic structure of these membranes provided in this study will enable a better understanding of the mechanisms of small molecule transport within these nanopores.

1 Introduction

More highly selective nanoporous membranes would be extremely useful for performing complex aqueous separations with seawater and various types of wastewater. For example, Sodium chloride and boron in seawater¹ and organic micropollutants found in municipal and

industrial wastewaters² represent just a few of the diverse contaminants of water sources. By efficiently separating contaminants from feed solutions with highly selective membranes, it is possible to reduce the number of required membrane passes and post-treatment steps needed for a given filtration process,³ thus lowering energy requirements. Additionally, one can also extract valuable resources from the feed streams. For example, flowback water produced during hydraulic fracturing of shale formations contains dissolved species such as acetate whose extraction has economic value.⁴

Reverse osmosis (RO) and nanofiltration (NF) are two prevailing membrane filtration processes that can be used to separate solutes on the order of 1 nm in size and smaller, including ions. However, commercially available amorphous RO membranes and porous NF membranes lack uniformity, which severely impacts their selectivity.⁵ Although scalable, their fabrication involves the spontaneous assembly of polymers into disordered structures that offer separation pathways that are tortuous and polydisperse in size.³ Tortuosity increases the effective length that a solute must travel, while pore size polydispersity limits membrane selectivity.

Ordered, nanostructured porous membrane materials have become an increasingly popular research area for aqueous separation applications because they offer the ability to control pore architecture at the molecular scale, thereby permitting the design of solute-specific separation membranes.⁶ However, their development has been limited by the ability to synthesize and scale various technologies. Graphene sheets are atomically thick, which results in excellent water permeability but defects during manufacturing severely impact selectivity.⁷ Molecular dynamics (MD) simulations of carbon nanotubes have shown promise,⁶ but synthetic techniques are unable to achieve scalable alignment and pore monodispersity.^{8,9} Consequently, there is a need for new materials that could provide scalable nanostructured porous membranes.

Preliminary evidence has shown that cross-linked lyotropic liquid crystal (LLC) membranes can be produced at moderate scale and may be capable of performing highly selective

separations. LLCs are amphiphilic molecules that have the ability to self-assemble into porous nanostructures¹⁰ and can be cross-linked to create mechanically strong membrane films with periodic pores on the order of 1 nm in diameter.¹¹ Unlike the pores in most commercial NF membranes, polymeric LLC membrane pores are uniform in size because they are formed by self-assembly. Since LLC polymer membranes lack an appreciable pore size distribution, they inherently exhibit high selectivity due to their strict molecular weight cut-off (MWCO).¹¹ Additionally, the LLC monomers examined in this paper are salts, and therefore lead to Donnan exclusion of ions in solution. The membrane gains a net surface charge when counterions from the head groups that line the pore walls escape into the feed solution in an effort to balance the gradients of concentration and electric potential.¹²

The feasibility of nanostructured LLC polymer membranes for selective separations has been demonstrated using LLC monomers that form the type I bicontinuous cubic (Q_I)^{13–15} and the inverted hexagonal (H_{II})¹¹ phases. When separating organic solutes from NaCl, Q_I -phase membrane filtration experiments have shown selectivity 2–3 times higher than commercial RO and 6–12 times higher than commercial NF membranes.⁴ When separating a series of various sized dyes, the H_{II} -phase membrane showed complete rejection of dyes bigger than 1.2 nm in size.¹¹

The H_{II} -phase pore geometry (Figure 1e) has a higher theoretical capacity for transport than the Q_I phase. The H_{II} phase forms at room temperature in the presence of ca. 10 wt% water and consists of hexagonally packed, hydrophilic pore columns.¹⁰ In the absence of water, neat monomer will form the same hexagonal columnar structure which, in the literature, has been referred to as the Col_h thermotropic phase.¹⁶ Q_I -phase membranes consist of a tortuous network of three dimensionally interconnected pores that prevent optimal through-plane transport. In contrast, the densely packed, non-tortuous and uniform sized pores of H_{II} -phase membranes represent the ideal geometry for achieving high solute flux.¹⁷ However, the hexagonally packed LC domains of the H_{II} -phase generally form mutually unaligned domains, which hurts membrane permeability. This domain scale misalignment

had inhibited further development of this technology, and research efforts were focused on the Q_I phase, whose geometry does not require alignment.¹⁸

However, recently researchers have learned how to macroscopically align the hexagonal domains which has revived research into H_{II}-phase LLC polymer membranes. In 2014, Feng et al. showed that one can align Col_h domains, created by the “dry” monomer Na-GA3C11, using a magnetic field with subsequent cross-linking to lock the structure in place.¹⁶ In 2016, Feng et al. showed that one could also obtain the same result by confining the neat monomer between PDMS or glass substrates since hexagonal mesophases preferentially anchor perpendicular to both surfaces.¹⁹ Current experimental efforts are focused on extending the method to the H_{II} phase and characterizing the performance of these newly aligned systems.

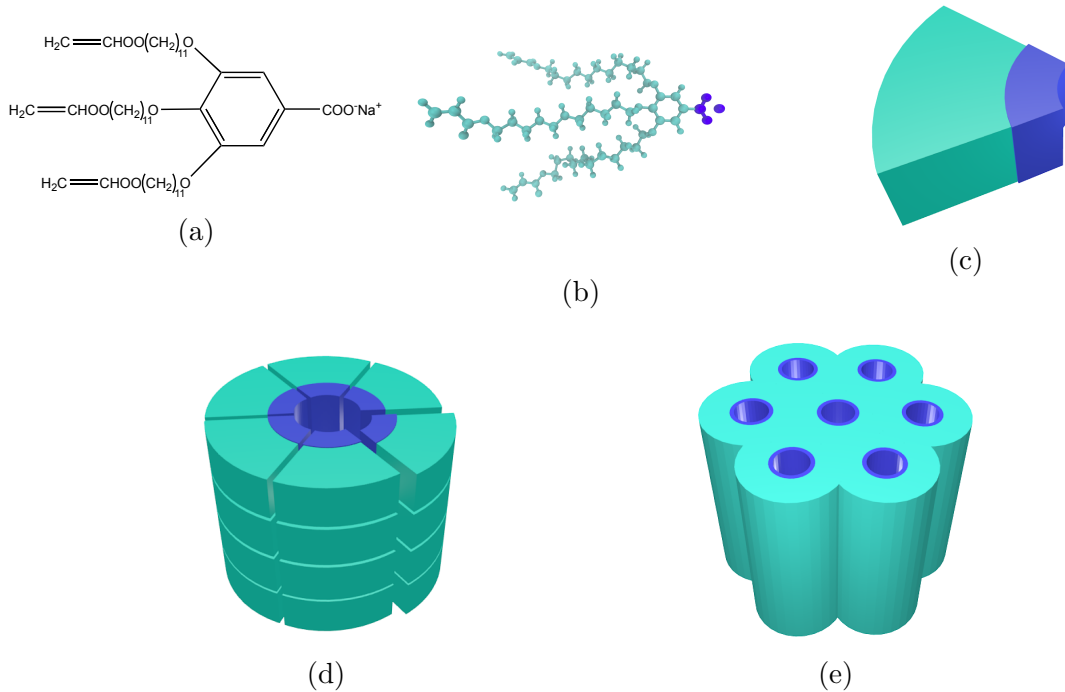


Figure 1: (a) The LLC monomer Na-GA3C11 (b) rendered atomistically (c) exhibits wedge-like character. (d) Monomers stack on top of each other to create columns with short range order, then assemble into pores with hydrophilic head groups (blue) facing towards the pore center. (e) The pores assemble into hexagonally packed columnar mesophases.

Our current understanding of the molecular details of resulting LLC polymer membranes'

nanostructure is not sufficient to be able to precisely design them for specific separations. Dischinger et al. attempted to use an empirical model that correlates the physiochemical properties of the counterion used in a Q_I-phase LLC membrane to solute rejection.²⁰ Although their model showed some qualitative agreement with experiment, the quality of fit of their model was limited due to complex solute-membrane interactions that could not easily be modeled. Additionally, they observed an unexpected discrepancy in the relationship between uncharged solute rejection and water permeability, which will require a more in-depth knowledge of the difference between solute and solvent transport.

Over the past 20 years, H_{II}-phase LLC polymer membrane studies have been limited primarily to the Na-GA3C11 monomer with some characterization done after minor structural modifications. For example, Resel et al. varied the length of the monomer tails and the counterion used and observed its effect on pore spacing.²¹ In a later study of rejection performance, it was shown that membranes formed by cross-linked Na-GA3C11 in the H_{II} phase cannot separate solutes less than 1.2 nm in diameter because the pores are too large.¹¹ We do not yet understand how to controllably reduce the effective pore size or how to tune the chemical environment in the nanopores of this or related materials for small molecule separations. The only source of predictive modeling for LLC systems have been macroscopic models that likely do not adequately describe transport at these length scales.¹³ Modeling with molecular detail could provide sufficient information about the mechanisms and chemical features to better inform experimental design of similar nanostructured membranes.

A molecular-level understanding of LLC polymer membrane structure, enabled by molecular dynamics (MD) simulations, will enhance our comprehension of the role of monomer structure in solute transport and provide guidelines to reduce the large chemical space available to design monomers for creation of separation-specific membranes. It is important that we model the system with a nanoscopic pore structure that is maximally consistent with experimental data in order to approximate the chemical environment experienced by solutes in future transport studies. Atomistic MD simulations can provide the required level of de-

tail (Figure 2b), assuming the force fields are sufficiently accurate. With such an atomistic model, we can directly observe molecular-level solute transport and suggest governing mechanisms. We can also observe how the choice of head group interacts with solutes of interest. In addition, we can interchange counterions which may influence both the pore size and the strength of the Donnan potential.

In this study, we achieve a more realistic atomistic description of hexagonal LLC polymer membranes than, to our knowledge, has ever previously been created, and explore what new structural information can be gained and what structure hypotheses are supported by this model. We validate the results using as much experimental information as possible. We are most interested in reproducing the conclusions about structure drawn from small-angle X-ray scattering (SAXS) and wide-angle X-ray scattering (WAXS) experiments, as well as in matching ionic conductivity measurements.¹⁹

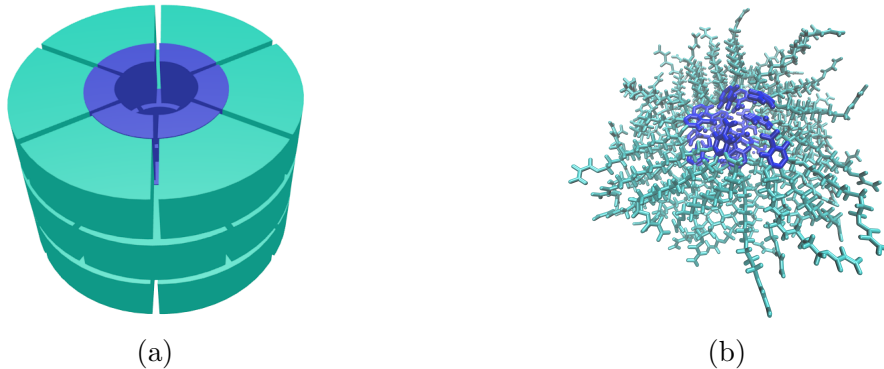


Figure 2: (a) Previous understanding of the pores are essentially speculations based on limited chemical and experimental data. (b) We use detailed molecular modeling in this paper in order to appropriately model the pore's complex architecture, which is crucial to understanding the mechanism of solute transport. In both pictures, the head group region is colored blue and the tail region is colored cyan.

In this paper, we perform molecular modeling of the Col_h thermotropic (i.e., solvent-free) assembly formed by Na-GA3C11. Compared to the lyotropic (i.e, solvent-containing) H_{II} phase, the Col_h phase is a simpler starting point. The system is not assembled in aqueous phase which allowed us to simulate longer timescales by omitting the solvent in

the simulations, and there exists detailed experimental characterization of the fully aligned state, including 2D-WAXS patterns (Figure 3a) that are useful for reconstructing structural data.

There are five major features of interest present in the 2D experimental WAXS pattern shown in Figure 3a.

1. *R- π* : The location of the first is at $q_z = 1.7 \text{ \AA}^{-1}$, corresponding to a real space separation of 3.7 \AA . Previous work attributes this reflection to π - π stacking between aromatic rings in the direction perpendicular to the membrane plane, or z -axis.¹⁶ For simplicity, we will refer to this reflection as R- π .
2. *R-double*: A weak intensity line, located at exactly half the q_z value of R- π ($q_z = 0.85 \text{ \AA}^{-1}$), corresponds to real space periodicity of 7.4 \AA . Since this reflection corresponds to double the spacing of R- π in real space, we will refer to it as R-double. R-double has been previously interpreted as 2_1 helical ordering of aromatic rings along the z -axis.¹⁶
3. *R-alkanes*: A low intensity ring located at $|\mathbf{q}| = 1.4 \text{ \AA}^{-1}$ marks the third major reflection of interest. The real space separation corresponds to 4.5 \AA which is characteristic of the average spacing between packed alkane chains.²² We will call this reflection R-alkanes.
4. *R-spots*: Within R-alkanes, are four spots of higher relative intensity. Accordingly, we name these reflections R-spots. The location of all spots is $\sim 37^\circ$ from the q_r axis in their respective quadrants. In many liquid crystal systems, such spots are explained as the result of alkane chains tilted with respect to the membrane plane.²³
5. *R-pores*: The final significant feature corresponds to the spacing and symmetry of the pore columns. The feature, which we named R-pores, is characterized by reflections along the equatorial axis defined by $q_z = 0$. The spacing between dots is indicative of the hexagonal symmetry of the packed pores. We observe the same information with

higher resolution by looking at the same system's 1D-SAXS pattern (Fig. 3b). The location of the leading SAXS peak (closest to $q_r = 0$) is related to the distance between pores.

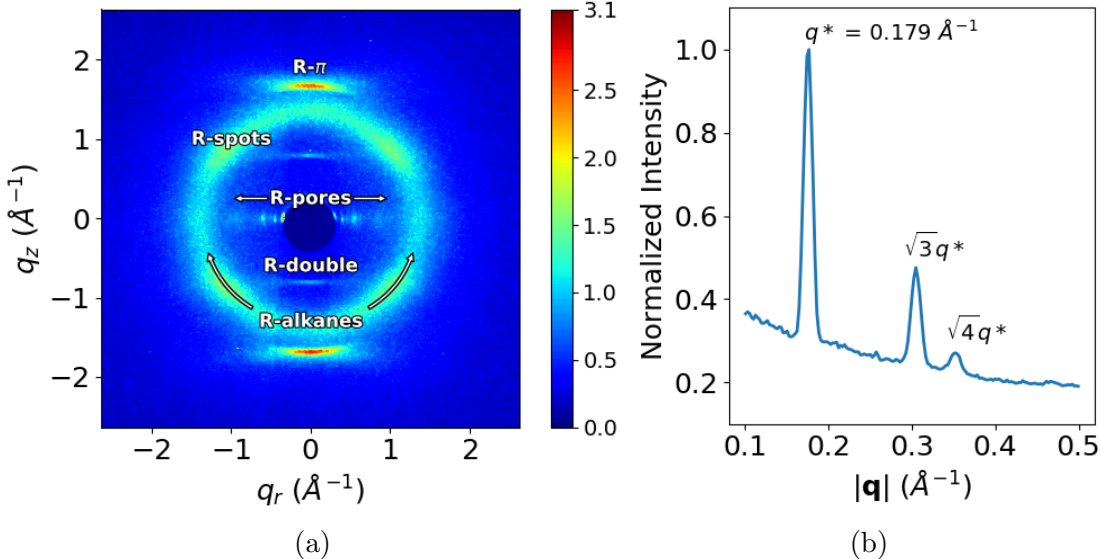


Figure 3: (a) 2D-WAXS gives details about repeating features on the order of angstroms. Experimentalists have explained each of the 5 major reflections present as follows: (R- π) Aromatic head groups $\pi - \pi$ stack 3.7\AA apart. (R-double) Monomers arrange vertically in a 2_1 helix. (R-alkanes) Alkane chain tails pack 4.5\AA apart. (R-spots) Monomer tails are tilted with respect to the membrane plane. (R-pores) As derived from SAXS, the pores are spaced 4.12 nm apart and pack hexagonally (b) (Reproduced from Ref. 19) The repeat spacing in the 1D-SAXS scattering pattern is characteristic of hexagonal packing. The leading peak, q^* , represents the distance between the d_{100} planes, which translates into a distance between pore centers of 4.12 nm .

Despite having structural data, there is still information which experiment cannot definitively answer. Specifically, we want to know:

1. What is the density of monomers that pack around each hydrophilic core?

Authors often describe this and similar systems as being made up of stacked monomer layers. A simple molecular simulation study of a similar molecule suggested that there are 4 monomers in each layer. Their estimation is based on a simulated system containing only 16 total monomers which likely does not sufficiently model the chemical

environment present in the real system.²⁴ A separate calculation based on the volume of the liquid crystal monomers proposes that there are seven monomers in each layer.²¹

We are careful to avoid the term “layers” since many liquid crystalline systems have long range order in 1 or 2 spatial dimensions and short range order in the other dimensions.²⁵ In the system we are studying, there are long-range 2D correlations in the hexagonal array of pores (*xy* plane) and short range *z*-direction correlations within stacked columns of monomers. In this study, we use atomistic molecular modeling to study how the system’s structure is affected by the density of these monomer columns that surround each pore’s hydrophilic core.

2. What structural motif best matches experimental 2D-WAXS patterns?

On the short timescales accessible to MD (even the 100’s of nanoseconds of simulation performed here are short compared to experimental timescales), we observe distinct metastable configurations which depend on starting configuration. We simulated X-ray diffraction (XRD) patterns of our system and compared them to experimental 2D WAXS patterns (Figure 3a) so that we ensure our model creates a nanoscopic chemical environment maximally consistent with experiment within the constraints of our force field. Using this approach, we are able to confirm some previous interpretations of the WAXS pattern and refute others.

3. Is it necessary to include any water in order to appropriately model the Col_h phase?

While the Col_h phase is described as dry, it is likely that small amounts of ambient water are absorbed into the system. The hydrogen-bonding network formed by the water may play a role in structuring the pore. We used simulated XRD patterns to uncover any meaningful structural difference between a “dry” and a “wet” system.

4. What is the detailed atomistic structure of the pores?

The limited picture that experiment provides tells us that there are hexagonally packed,

hydrophilic regions where transport is likely to occur. One may instinctively imagine these regions as tube-like pathways with well-defined boundaries. We explored the composition of the pores, the partition between the hydrophilic and hydrophobic regions, and its sensitivity to initial configuration, including both dry and wet systems.

2 Methods

2.1 Source code

Python scripts used to set up systems and conduct post-simulation trajectory analysis are available online at <https://github.com/bencoscia/l1csm>. The python scripts used to simulated XRD patterns are publicly available online at <https://github.com/joeyelk/MD-Structure-Factor>. Additional details are available in Section S1 of the Supporting Information (SI).

2.2 Monomer Parameterization

We parameterized the interaction potential for the liquid crystal monomer Na-GA3C11 using the Generalized AMBER Force Field (GAFF)²⁶ with the Antechamber package²⁷ provided with AmberTools16.²⁸ We chose GAFF because it has been parameterized for use with organic molecules. Although researchers have optimized force fields, including GAFF, for use with liquid crystals, they are often tuned in order to reproduce one or more experimental observables for specific types of liquid crystal molecules.^{29,30} Since liquid crystals exist in a wide range of shapes and sizes, including candidate monomers which we may study, we chose to stick with a widely used force field. If we can reproduce experimental trends using a single ‘out-of-the-box’ force field, then there will be no need to complicate our studies with customized parameter sets. We assigned atomic charges using the am1bccsym method of `molcharge` shipped with QUACPAC from Openeye Scientific Software. We ran all molecular dynamics simulations using GROMACS 2016.^{31–34}

We generated an ensemble of characteristic, low-energy vacuum monomer configurations by applying a simulated annealing process to a parameterized monomer. We cooled monomers from 1000 K to 50 K over 10 ns. We randomly pulled a low energy configuration from the trajectory then reassigned charges using `molcharge`. Using the new charges, we annealed the monomer system again and pulled a random monomer configuration from the trajectory which we used for full system construction. Section S2 of the SI provides further detail of the parameterization process.

2.3 Unit Cell Preparation

The time scale for self-assembly of monomers into the hexagonal phase is unknown and likely outside of a reasonable length for an atomistic simulation, requiring a more efficient way to build the system. Previous work has shown that a united-atom model of an LLC can self-assemble into the H_{II} phase configuration in ∼1000 ns.³⁵ We attempted atomistic self-assembly by packing monomers into a box using Packmol.³⁶ Simulations of greater than 100 ns show no indicators of progress towards an ordered system (see Section S3 of the SI). To bypass the slow self-assembly process, we used automated procedures to assemble monomers into a structure close to one of a number of hypothesized equilibrium configurations (See Figure S3 of the SI). These initial structures may result in equilibration into slowly-interconverting metastable states, an issue we will address later in the paper.

A typical simulation volume contains four pores in a monoclinic unit cell, the smallest unit cell that maintains hexagonal symmetry when extended periodically. Each pore is made of columns of stacked monomers with periodic continuity along the pore axis, avoiding any edge effects and creating an infinite length pore ideal for studying transport. We prefer a small number of stacked monomers in order to reduce computational cost and to allow us to look at longer timescales. Ultimately, we chose to build a system with 20 monomers per column in order to minimize finite size effects with reasonable computational expense and to obtain sufficient resolution when simulating XRD patterns (see further discussion in Section

S5 of the SI).

2.4 Monomer Placement

When constructing an initial configuration, there are a number of variables which require careful consideration while placing monomers. We find that the equilibrium configuration is sensitive to some while insensitive to others. For example, we find the starting pore radius, defined as the distance of a chosen head group carbon from the pore's central axis, does not influence the equilibrium structure if one chooses a reasonable value. The initial distance between pores, within a wide range, also has little effect on the equilibrated structure. However, one should not start them too close or there will be high energy repulsions during early equilibration. We chose a pore radius of 0.5 nm and an initial pore spacing of 4.5 nm, \sim 10% larger than the experimental value of 4.12 nm for our initial configurations. A sensitivity analysis of both parameters is presented in the SI, Section S6. The distance between vertically stacked monomers, the *xy* position of monomers with respect to vertically adjacent monomers, and the number of columns per pore do influence the equilibrated structure and require further justification for their choices. We rely on experimental data to inform them.

We chose the vertical spacing between monomers for the initial configuration based on R- π and then allowed the system to readjust during equilibration. We rotated each monomer so the plane of its aromatic head group would be coplanar with the *xy* plane. We explored three different initial monomer spacings. The first is exactly equal to R- π with monomers placed so aromatic rings stack 3.7 Å apart in the *z*-direction. We also extensively explored a second system with an initial spacing of 5 Å. We briefly explored a third system with an initial spacing of 10 Å. However this largest spacing yields non-physical behavior which is detailed in the SI, Section S6.3.

We chose the relative orientation between vertically adjacent monomers in each column based on clues from diffraction data as well as the various known stacking modes of benzene and substituted benzene rings: sandwiched, parallel displaced and T-shaped.³⁷ We ruled out

the T-shaped configuration because its ~ 5 Å equilibrium stacking distance³⁷ is inconsistent with R- π . It is also infeasible for the monomers to orient in the T-shaped conformation because of the bulky tail groups. We explored the system's preference towards the sandwiched vs. parallel displaced stacking modes in some detail. Both have reported stacking distances near the R- π value of 3.7 Å. Head groups in our sandwiched initial configuration stack directly on top of each other while head groups in the parallel displaced initial configuration stack with an offset of $180^\circ / n_{col}$ where n_{col} is the number of columns per pore. See Figure S9 of the SI for a detailed illustration of the initial configurations in each mode.

The number of columns per pore is unknown, as stated in Question (1). We tested configurations constructed with a varied number of columns per pore. We built systems in the sandwiched and parallel displaced configurations with 4, 5, 6, 7 and 8 columns per pore.

2.5 Equilibration

We developed equilibration schemes for creating dry (i.e. thermotropic LC phase) and wet (i.e. LLC phase) configurations. Both schemes start with an initial configuration generated according to the previous guidelines. For wet systems, we added the desired concentration of water to the initial configuration and carried out equilibration in the same way as the dry systems. First, we fixed monomer head groups in place using position restraints with a force constant of 10^6 kJ mol⁻¹ nm⁻². We gradually released the position restraints by decreasing the force constants over a series of NVT simulations. We allowed the resulting unrestrained structure to equilibrate for 5 ns in the NPT ensemble with pressure controlled by the Berendsen barostat, followed by NPT equilibration simulations run for at least 400 ns using the Parrinello-Rahman barostat. More equilibration details are given in Section S8 of the SI.

2.6 Equilibrium Calculations

2.6.1 Determining Equilibration Time

Using equilibrated structures, we carried out various calculations to characterize the system. We defined the point at which a system is equilibrated based on when the distance between pores stopped changing. We determined when the distances stopped changing by applying the statistical test of Chodera,³⁸ implemented as `pymbar.timeseries.detectEquilibration`, to the time series. Typically, the pore-to-pore distance equilibrated between 200 and 350 ns. We used data collected after equilibration to do all subsequent analysis.

2.6.2 Calculation of Pore Spacing

To calculate the equilibrated pore spacing, we measured the distance between pore centers. We located the pore centers by averaging the coordinates of sodium ions in their respective pores. We generated pore spacing statistics using the bootstrapping technique (See Section S9 of the SI). The pore spacings calculated in this way are consistent with one half of the x and y box vectors (See Table S3 in the SI). However, our method for their calculation does a better job capturing the spread of pore-to-pore distances.

2.6.3 Generation of Simulated X-ray Diffraction Patterns

We generated simulated XRD patterns based on atomic coordinates in order to make a direct experimental comparison. We modeled all atomic coordinates as Gaussian spheres of electron density whose maximum and width are defined by each atom's atomic number and electronic radius respectively. A three dimensional Fourier transform of the array of electron density results in a three dimensional structure factor which represents the unit cell in reciprocal space. The experimental WAXS measurement was made using a vertically aligned film whose pores were oriented perpendicular to the direction of the incident X-ray beam. Although the pores are vertically aligned, the crystalline domains are still misaligned

with respect to the xy plane. To account for this, we averaged 2D slices of the structure factor at all angles about $\mathbf{q} = (0, 0, z)$.

We normalized all diffraction patterns relative to R-alkanes. We believe that the alkane-alkane density, averaged over all angles, is the feature most likely to be replicated between experiment and simulation, as atomistic alkane force field parameters are relatively well-studied.²⁶ Other features are dependent on system ordering which is likely to have some dependence on initial configuration. We calculated the average intensity within R-alkanes of the experimental pattern, I_{avg} , and divided all intensities by this value. In this way, the average intensity of R-alkanes was set equal to 1. When calculating I_{avg} , we excluded intensities within $\pm 30^\circ$ of the meridional axis defined by $q_r = 0$, since the simulated patterns differ from experiment in those regions in all cases (See Figure 4a). Specifically, in contrast to the experimental WAXS pattern, R- π , as it appears in the simulated diffraction patterns, intersects with R-alkanes (See Section 3.2.4). We set an upper bound on the colorbar by multiplying I_{avg} by a scaling factor, f . Intensities that appear in the patterns $\geq f \times I_{avg}$ are colored uniformly. We applied the same scaling method to the simulated patterns. We chose a scaling factor of $f = 3.1$ in order to visibly display all features in all patterns.

We reported the intensities of R- π and R-double by recording the maximum values of the peaks of the q_z cross-section of the experimental pattern at $q_r = 0$ (Figure 4b). In the case of the experimental pattern, the peak heights are not perfectly symmetrical, so we report the average of the two heights.

We measured the intensity of R-spots by averaging the peak heights produced by radially integrating the patterns within the R-alkanes region (Figure 4c). In some patterns, the spots are not easily discernable due to obstruction by other features. In that case, we report the average intensity at the intersection of R-alkanes with the q_z value of R-double since that is where we expect it to appear based on experiment. Since R-double does not appear in our simulated patterns, we estimate where it should appear as half of the q_z value of R- π .

We measured the intensity of R-pores based on the intensity of the d_{100} peak (the leading

peak closest to $q_r = 0$) of the q_r cross-section of the patterns at $q_z=0$ (Figure 4d). The beamstop covers most of the small angle reflections in the experimental 2D-WAXS pattern. In order to compare the simulated intensity of R-pores to experiment, we used the q_r cross-section of 2D-SAXS which was generated from the same sample (Figure S11 of the SI). Since the d_{200} peak is partially exposed in the experimental 2D-WAXS pattern, we normalized the experimental 2D-SAXS cross-section by matching the intensity of the d_{200} peak between it and the experimental 2D-WAXS cross-section. It is possible that the peak is not fully captured in the 2D-WAXS pattern and that we have underestimated the intensity of R-pores in the experimental pattern.

2.6.4 *Pair Distribution Functions and Correlation Length*

The normalized pair distribution function, $g(\mathbf{r})$, describes the probability of finding a pair of particles separated by \mathbf{r} ,

$$g(\mathbf{r}) = \frac{1}{\rho N} \left\langle \sum_{i=1}^N \sum_{j \neq i}^N \delta(\mathbf{r} + \mathbf{r}_j - \mathbf{r}_i) \right\rangle \quad (1)$$

where ρ is the average number density of particles and $\delta(\mathbf{r})$ is the Dirac delta function.³⁹ We applied Equation 1 in three dimensions and then extracted one dimensional distribution functions using slices of the grid along the appropriate axis.

We measured the one dimensional pair distribution function, $g(z)$, between centers of masses (COMs) of aromatic head group rings along the z -axis (perpendicular to the membrane plane). We averaged all 1D z -directional slices of the full 3D correlation function within 2.1 Å of $(x, y) = (0, 0)$. We chose 2.1 Å as a crude approximation of the radius of the phenyl ring plane. We calculated the radius as the sum of the longest C-C distance within a phenyl ring (2.8 Å) and two times the carbon atom electronic radius (0.7 Å).⁴⁰ In this study, $g(z)$ is characterized by an oscillatory function with a period equal to the average distance between stacked monomers, and an amplitude that decays exponentially (see Section 3.2.4). The rate

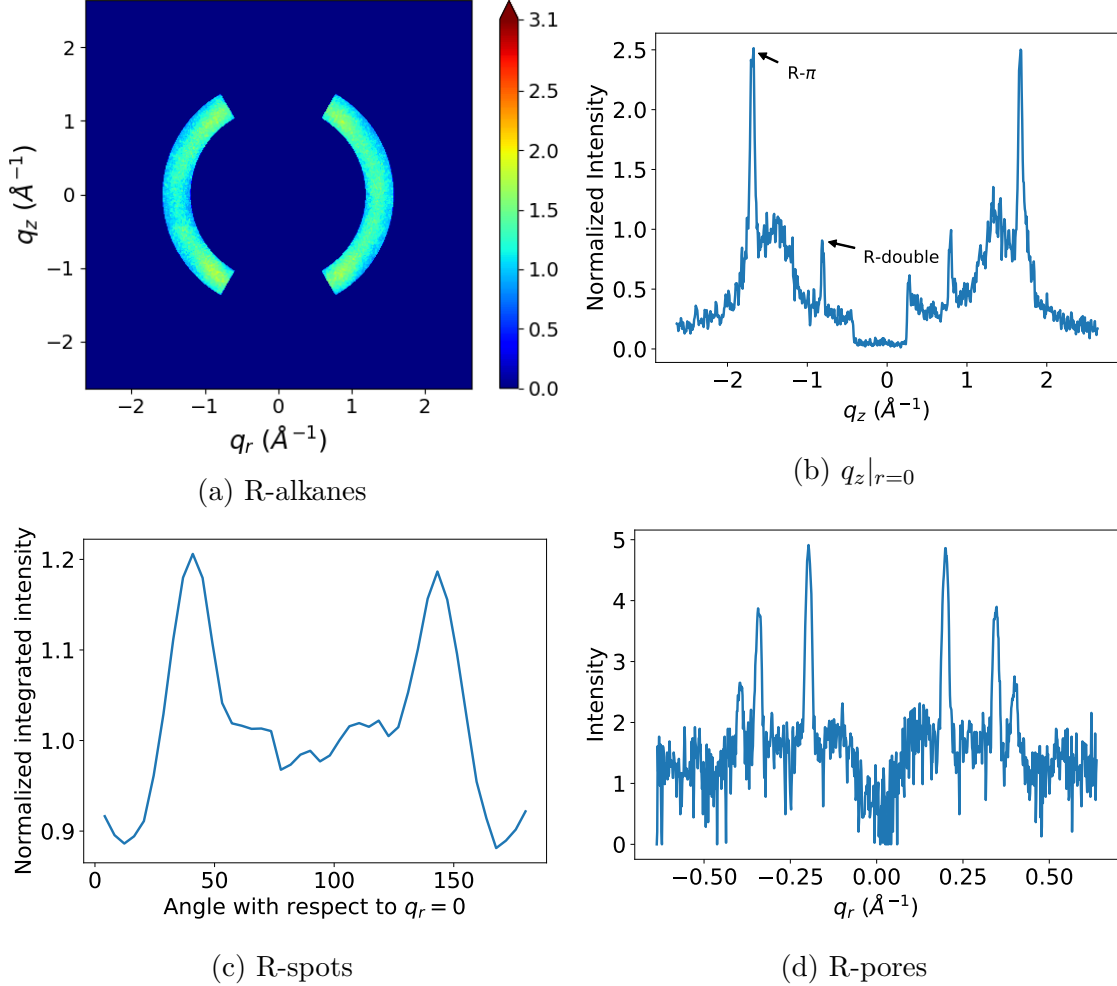


Figure 4: (a) We measured the intensity of R-alkanes by calculating the average intensity within the region bounded by $|\mathbf{q}| = 1.4 \text{ \AA}^{-1}$ and 1.57 \AA^{-1} (between 4.0 and 4.5 \AA in real space). We excluded intensities within $\pm 30^\circ$ of the meridional axis defined by $q_r = 0$, since the simulated spectra overlap with R- π in those regions in all cases. (b) We measured the intensity of R- π and R-double based on the peaks of the q_z cross-section of the diffraction pattern. (c) We measured the intensity of R-spots by averaging the peak heights produced by radially integrating the patterns within the R-alkanes region. We took the intensity of R-spots as the average of the peak intensities near 37 and 143° . (d) We measured the intensity of R-pores by measuring the height of the d_{100} peak (the leading peak closest to $q_r = 0$) of the cross-section of the diffraction patterns along the q_r axis at $q_z = 0$.

of decay is related to the correlation length, L , between monomer head groups. We estimated L by fitting the peaks of $g(z)$, using the python package `scipy.optimize.curve_fit`,⁴¹ to

a decaying exponential function of the form:

$$Ae^{-z/L} \quad (2)$$

where A is a fitting parameter for amplitude, z is the independent variable of $g(z)$, and L is the fit correlation length. We calculated the error in the estimated value of L as the square root of the diagonal entry of the covariance matrix of optimized fit parameters.

We also used $g(z)$ to calculate the equilibrated vertical stacking distance between monomers, d_{equil} . We fit a decaying sinusoidal function (using `scipy.optimize.curve_fit`) to $g(z)$ of the form:

$$1 - A \cos\left(\frac{2\pi}{d_{equil}}z + B\right) e^{-z/L} \quad (3)$$

where A and B are fit parameters for the function's amplitude and phase shift respectively. This function could be used in place of Equation 2, however it does not consistently fit the peaks of $g(z)$ from parallel displaced configurations well enough to extract a reliable value of L.

2.6.5 Radial Distribution Functions

We explored the pores' compositions by measuring the average number densities of various monomer components as a function of distance from the pore centers. We looked at the average number density of sodium ions, aromatic rings and carbon atoms making up the monomer tails. We binned the radial distance of all atoms in each group from the pore centers, then normalized by the volume of the annulus defined by the bin edges and the z box vector (See Figure S14 of the SI).

2.7 Simplified Systems

In order to gain a deeper understanding of discrepancies between the experimental and simulated R- π reflection, we used a simplified model where we represent each monomer as

a single point scatterer located at the COM of its head group. In order to make a system approximately similar to our equilibrated simulation geometries, we created 4 hexagonally packed pore regions spaced 42.5 Å apart, each with 5 columns of scatterers spaced 4.4 Å apart in the z -direction. We built the system 4 times taller in the z -direction (80 scatterers per column) in order to access higher q_z resolution.

We gave the simplified models the same amount of disorder present in the atomistic simulations. We observe two sources of disorder in our atomistic simulations: thermal motion of atoms during the simulation and quenched disorder created by rapid structural rearrangement during early equilibration that is largely locked into place for the remainder of the simulation, even at the 100 ns time scale. We measured thermal disorder by calculating the standard deviation of the distribution of head group COM positions from their average positions. We measured quenched disorder by calculating the standard deviation of the distribution of head group COMs from their idealized average positions. In the z -direction, we measured the deviation of the head group COMs from an equally spaced column of head groups. In the xy plane, we calculated the standard deviation in radial position from the pore center and the angular deviation from equally spaced points surrounding the pore center. This method for calculating quenched disorder inherently includes the convoluted thermal disorder.

We approximated interactions between particles by correlating the z -distance between points within each column of point scatterers. We placed points in each column by drawing random samples from a multivariate normal distribution defined by the mean positions of an equally spaced column of points. We gave the distribution at each point along the column the same standard deviation, σ_z , and we defined a covariance matrix such that the covariance, v , of the distance, d , between scatterers decays exponentially from v according to the equation $ve^{-d/L}$, where L is the correlation length. Unless noted otherwise, we used the experimental correlation length of 9.0 Å.

We calculated averaged R- π profiles by simulating the diffraction pattern of trajectories

consisting of 1000 independent simple system configurations generated with point scatterer placement based on the quenched disorder seen in atomistic simulations. The quenched disorder observed in the atomistic simulations is up to 8 times greater in magnitude than thermal disorder (See Table 3 in Section 3.2.4). This method for simulating time-averaged R- π profiles assumes that the timescales for large scale rearrangements of the system are much longer than what we can feasibly simulate with MD.

2.8 Ionic Conductivity Calculations

We calculated ionic conductivity using the Nernst-Einstein relationship, which relates the DC ionic conductivity, σ , to ion diffusivity, D , concentration, C , ion charge, q , the Boltzmann constant, k_b , and absolute temperature, T :

$$\sigma = \frac{q^2 C D}{k_b T} \quad (4)$$

We measured sodium ion diffusion coefficients by calculating the slope of the linear region of the z -direction mean square displacement curve as indicated by the Einstein relation.⁴² We visualized the MSD plot to determine where to begin and end a linear fit. We measured ion concentration with respect to the volume of the entire unit cell. More details are provided in the SI, Section S12.

2.9 Cross-linking

In order to better match the experimental membrane synthesis process, we created a cross-linking algorithm that one can apply to equilibrated structures. The primary purpose of cross-linking experimentally is to create a mechanically robust membrane. For that reason, we are not concerned with replicating the kinetics of the reaction, but instead emphasize understanding how much and in what way cross-linking modulates the system's structure.

We based our cross-linking algorithm on the known reaction mechanism (Figure S16 of

the SI). The reaction takes place at the terminal vinyl groups on each alkane tail. The procedure is carried out iteratively. Each iteration, the algorithm chooses carbons to cross-link based on the distance between eligible carbon pairs. The algorithm then updates the topology with the new bonds and atom types, energy minimizes the system and runs a short simulation before selecting the next group of eligible carbons atoms.

3 Results and Discussion

3.1 Density of Monomers Around Pores

Our simulations best support a model built with 5 monomer columns per pore based on the measured equilibrated pore-to-pore distances. To identify the density of monomer columns around each pore, addressing Question 1 in the introduction, we ran simulations of systems created with 4–8 columns per pore. We built systems in both the parallel displaced and sandwiched configurations and equilibrated them according to the dry equilibration procedure. We tested all systems with an initial vertical monomer spacing, d , of 3.7 Å in accordance with R- π . We tested 4 additional systems with monomers initially spaced 5 Å apart vertically (see Section S6.1 of the SI for more details on sensitivity to initial monomer spacing). We considered the pore-to-pore spacing to be equilibrated as defined in Section 2.6.1. Figure 5 shows the equilibrated pore-to-pore distances for all systems tested.

All systems tested, although equilibrated from the perspective of the metrics used here, are frozen in metastable basins. Not all make physical sense or fit the experimental profile that we are trying to match. In the limit of infinite simulation time, all systems will in theory converge to a single equilibrium configuration, but that time is far beyond the 100's of nanoseconds simulated here. For simplicity, we group the systems studied here into the ordered and disordered basins. What we find is that any system equilibrated with $d = 3.7$ Å can generally be characterized as being in a more ordered basin, and any system equilibrated with $d = 5.0$ Å can be characterized as being in a more disordered basin. The extra

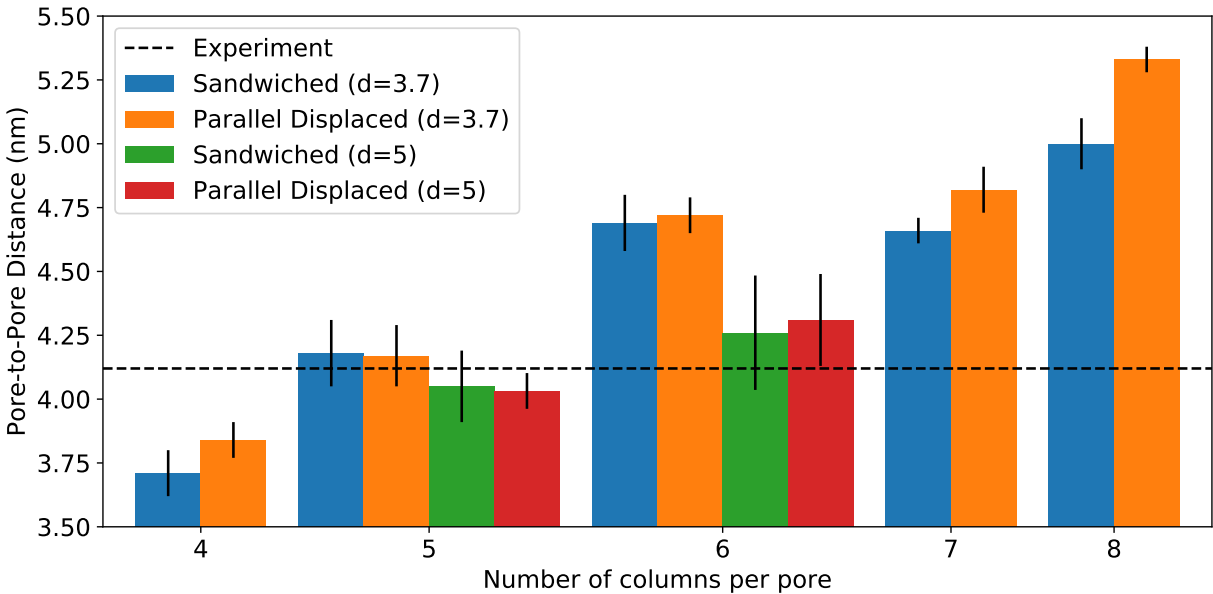


Figure 5: Systems with 5 columns per pore have equilibrated pore spacings closest to the experimental value of 4.12 nm. The equilibrated pore spacing of the model increases as the number of columns in each pore increases.

space between stacked monomers in the disordered basin systems gives the monomer head groups more rotational freedom. We quantified the ordering of the head groups using the nematic order parameter (see Section S14 for details of the calculation). Disordered basin systems have a lower nematic order parameter (meaning they are more disordered) than ordered basin systems. Generally, when monomers are started further apart, they stay further apart than systems where monomers are started closer together (see Table 2). This increased equilibrated stacking distance of monomers in disordered basin systems increases their discrepancy with experimental stacking distances derived from WAXS relative to ordered basin systems (See Section 3.2.4).

Systems built with 5 columns around each pore equilibrate to a pore spacing that is most consistent with the experimental value of 4.12 nm derived from SAXS measurements (Figure 3b). Ordered basin systems built with 4 columns per pore equilibrate to an average pore spacing 0.25 nm lower than experiment. Ordered basin systems built with 6 columns per pore, have an equilibrated pore spacing ca. 0.50 nm higher than experiment. Monomers in

disordered basin systems built with 6 columns-per-pore agree with experimental pore-to-pore distances within error, but stack too far apart. 6 column per pore disordered sandwiched and disordered parallel displaced configurations stack ~ 4.87 and 4.94 \AA apart respectively, which is $\sim 1.2 \text{ \AA}$ further apart than suggested by experiment. 5 column-per-pore systems stack, at a maximum, 0.9 \AA further apart than experiment (see Table 2). The remainder of this discussion will therefore focus on the analysis of systems built with 5 columns per pore.

The number of columns per pore dictates the density of interaction sites within each pore and the pore radius. A higher number of interaction sites will surely play a role in transport of molecules that have an affinity for the monomer head groups. The pore radius increases with the number of columns per pore (See Figure S19). This radius is likely related to the size of the molecules which can be excluded by this type of membrane. One may be able to control LLC membrane pore size by selecting monomers that are stable in configurations with more columns-per-pore.

3.2 Simulated XRD Comparison to 2D-WAXS Data

We can better understand the structure of the system by simulating XRD patterns produced from equilibrated MD trajectories (see Section 2.6.3) and comparing these simulated patterns to experiment, addressing Question 2 in the Introduction. We tested systems built with 5 columns per pore in the parallel displaced and sandwiched configurations at 300 K in the ordered and disordered basins, as those were the most consistent with the most unambiguous XRD features, the pore-to-pore spacing and the stacking distance, as described in Section 3.1. We generated simulated patterns using the locally equilibrated portion of each simulation trajectory (see Section 2.6.1). There are two important factors to take into account when looking at differences between experimental and simulated XRD patterns. First, the simulated diffraction patterns have some noise, especially along the q_z axis at $q_r=0$, which is where several of the more interesting features are located. This is due to the angle averaging of the 3D structure factor around the q_z -axis, meaning there are fewer

samples as q_r approaches 0. More importantly, our simulations do not appear to be long enough to sample truly independent configurations within their respective metastable basins (see Section 3.4), meaning we must take care in interpreting the results of the XRD. The amount of independent configurations required to converge along the q_z axis is analyzed in SI, Section S16. The simulated patterns generated for all systems studied are shown and compared to experiment in Figure 6.

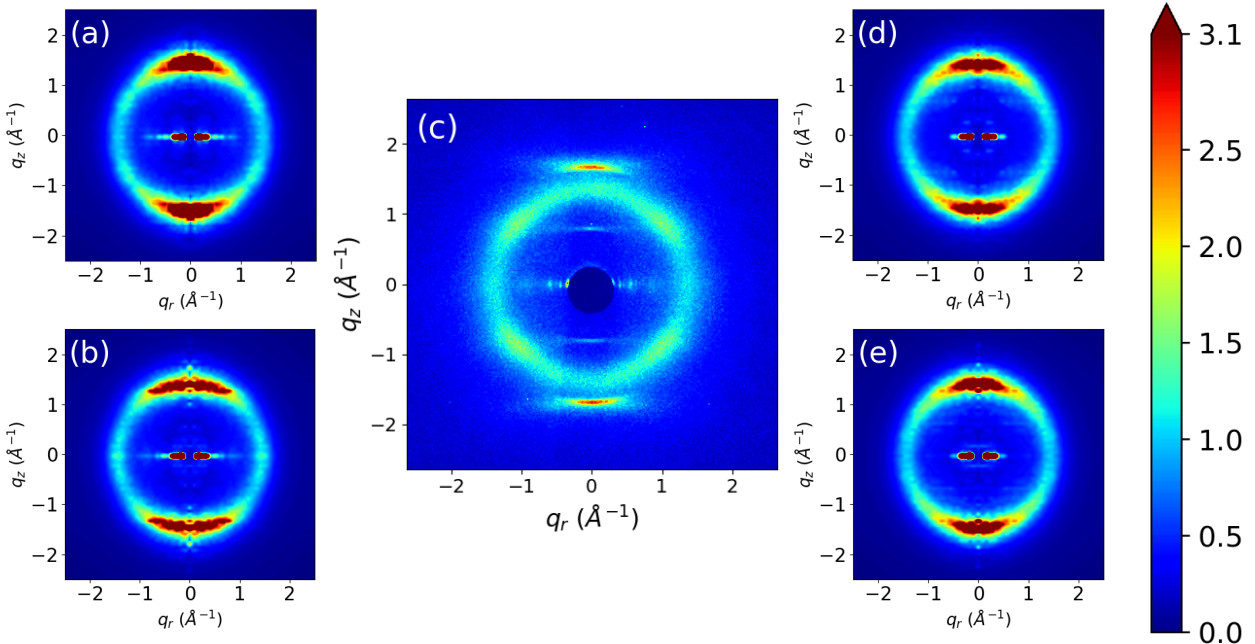


Figure 6: Simulated XRD patterns show some qualitative agreement with experiment. Shown is a comparison of the (a) Sandwiched, ordered basin (b) Sandwiched, disordered basin (d) Parallel displaced, ordered basin and (e) Parallel displaced, disordered basin configurations with (c) experimental WAXS. The major reflections of interest (See Figure 3a for their definitions) are present at varying degrees. In all cases, R-pores, R-alkanes and R- π are present to some degree. R-spots is also present, however it is generally partially covered by the broad R- π reflection. Quantitative comparisons of the relative intensities and locations of reflections of interest are presented in Table 1. In both XRD patterns generated from parallel displaced configurations, there is a faint line across $q_z \sim 0.7 \text{ \AA}^{-1}$, half the simulated value of R- π . Although it does not cross through $q_r = 0 \text{ \AA}^{-1}$, it is at the same q_z value where we expect R-double to be present. Still, R-double is not fully reproduced in any of the simulated patterns.

The simulated XRD patterns show moderate agreement with experiment. There are key qualitative and quantitative differences between the experimental and simulated locations

and intensities of each major reflection. The integrated intensity and location of each simulated reflection relative to its experimental counterpart are shown in Table 1. Our approach for measuring the intensity of each reflection is described in Section 2.6.3.

In the next few subsections, we individually address each major reflection, and the similarities and differences between simulation and experiment. We start with relatively uncomplicated analyses of reflections that are very similar between experiment and simulation:

- The location of R-alkanes (Section 3.2.1)
- The location and intensity of R-pores (Section 3.2.2)

and then move onto more complicated explanations of those reflections whose characteristics do not match, or have not been fully explained by experiment:

- The origin of R-spots (Section 3.2.3)
- The position, shape and intensity of R- π (Section 3.2.4)
- The origin of R-double (Section 3.2.5)

3.2.1 The Location of R-alkanes

We normalized the experimental and simulated diffraction patterns so that the average intensity within R-alkanes is equal to 1 because we believe that R-alkanes is the experimental feature most likely to be reproduced by our simulations. We reached this conclusion because alkane parameters in GAFF and AMBER force fields generally reproduce data well.^{26,43}

R-alkanes appears close to its expected location. In all cases, the maximum intensity of R-alkanes along the q_r axis at $q_z=0$, which we use to estimate its location, appears at a $|\mathbf{q}|$ value that is, at most, 3.5% higher than experiment. The error in the simulated diffraction patterns is less than the error due binning in each frequency direction, so was not further investigated.

Table 1: The simulated XRD patterns of the systems tested, normalized so that the average intensity of R-alkanes in each pattern equals 1, show R-pores and R- π reflections that are significantly higher than experiment and R-spots reflections that are slightly lower than experiment. R-double does not appear in any simulated patterns, and thus has no measurable intensity. In terms of the locations of the reflections, R-pores, R-alkanes and R-spots appear at $|q|$ values that are close to experiment, while R- π appears at a significantly lower $|q|$ value than experiment.

Reflection	Normalized Reflection Intensity					
	Experiment	Sandwiched	Parallel	Disordered	Disordered	
			Displaced	Sandwiched	Parallel	Displaced
R-alkanes	1.0	1.0	1.0	1.0		1.0
R-pores	4.91	49.5	54.0	50.8		53.4
R-spots	1.2	1.2	1.2	1.1		1.1
R- π	2.8	44.0	7.7	8.4		10.1
R-double	0.9	—	—	—		—
Reflection	Reflection Location ($ q \text{ \AA}^{-1}$)					
	Experiment	Sandwiched	Parallel	Disordered	Disordered	
			Displaced	Sandwiched	Parallel	Displaced
R-alkanes	1.39	1.44	1.44	1.42		1.43
R-pores	0.176	0.170	0.170	0.173		0.172
R-spots	1.39	1.44	1.44	1.42		1.43
R- π	1.70	1.41	1.42	1.40		1.40
R-double	0.85	—	—	—		—

3.2.2 The Location and Intensity of R-pores

R-pores is about 10 times more intense than experiment in all simulated systems. Some or all of this discrepancy may be a consequence of our normalization of the experimental 2D-SAXS pattern, since the common peak between it and the 2D-WAXS patterns is partially obscured by the beamstop in the WAXS. If our simulations do indeed predict an intensity of R-pores that is too high, we hypothesize that this is primarily due to the relatively perfect infinite hexagonal array of pores in the simulated systems. In the real system, periodicity of the hexagonal array is disrupted by misalignment of the crystalline domains and the pore-to-pore distances fluctuate more over long time scales. The agreement in intensity in R-pores obtained here is sufficient for this study because this intensity is primarily controlled by

longer-range organization that cannot be captured by simulation of only 4 pores and because we are only concerned with the structure of the individual pores themselves.

The location of the leading peak of R-pores is directly related to the average distance between pores. However, there is substantial uncertainty in the exact location relative to the bin size resulting from the Fourier space transformation. We can instead measure the average distance between columns with more precision in real space (See Section 2.6.2). We showed that we achieve experimentally consistent pore spacings in our simulations in Section 3.1.

3.2.3 The Origin of R-spots

The intensity of R-spots is close to experiment when generated from any of our simulated systems. We measured its intensity as outlined in Section 2.6.3.

In order to more clearly identify the structural reasons for R-spots, we equilibrated an ordered basin sandwiched configuration at 280 K to moderately increase the order and therefore intensity. Many force fields do not obtain the correct equilibrium structure at precisely the experimental temperature. Wang et al. highlighted the shortcoming of some of the most popular protein force fields in predicting the temperature dependence of protein structural ensembles.⁴⁴ It is therefore possible that our membrane system, simulated at 300 K, is understructured in the tail region compared to the experimental structure at 300 K. We found that lowering the temperature indeed better resolved R-spots (Figure 7a), suggesting that our ‘effective’ temperature might indeed be too high, understabilizing structure.

Previous literature has attributed the R-spots reflection in this particular WAXS dataset as the result of tilted alkane chains.¹⁶ This explanation is not unfounded as there are examples in literature of systems where tilted liquid crystals give rise to reflections that resemble R-spots.^{45,46} We measured the tilt angle of the alkane chains of the 280 K system by measuring the angle made by the vector extending from top to bottom of each tail with respect to the membrane plane. We found that it equilibrates to an average tilt angle of $-2 \pm 13^\circ$ (Figure 7b), far from the 37° tilt angle previously used to explain R-spots. Even when

we placed position restraints on the monomers in a tilted initial configuration, monomers quickly reduced their tilt relative to the xy plane to an angle statistically indistinguishable from zero (see Section S17 of the SI).

The evidence from simulations strongly suggest that the source of the R-spots reflection is packing of the tails in a hexagonal array. First, we demonstrate R-spots comes primarily from the tails, by removing all non-tail atoms from the trajectory and simulating the XRD pattern with the remaining atoms, which preserves R-spots (Figure 7c). Next, we plotted the center of masses of the first four tail atoms of all tails (Figure 7d). We measured the angle between each COM and its nearest neighbor COMs with respect to the xy plane of the membrane. We see distinct peaks in the distribution of these angles located ca. -60° , 0° , and 60° , which is consistent with a hexagonally-packed configuration (Figure 7e). This ordering is primarily in the parts of the tail proximal to the heads, and dies off at the tail ends, where there is more space to fill causing them to pack nearly isotropically. See Section S18 of the SI for a more detailed explanation of the calculation and packing distributions generated from different sections of the tails.

The peaks in the nearest neighbor angle distribution due to the hexagonal packing are consistent with the location of R-spots. The 2D-Fourier transform of a simple hexagonal array constructed based on the peak angles in Figure 7e shows reflections in the same locations as R-spots, in addition to vertical stacking reflections along the q_z axis that would intersect with R- π (Figure 7f).

3.2.4 The Position, Shape, and Intensity of R- π

The position, shape, and intensity of R- π , generated from simulations at 300 K have qualitative and quantitative differences from experiment. The reflections appear at lower q_z values, they are more intense, and the shape of its cross-sections, especially in the q_r direction are different relative to the experimental system. For comparison, see Figure 8 where we used cross-sections of the simulated XRD generated from the ordered parallel displaced

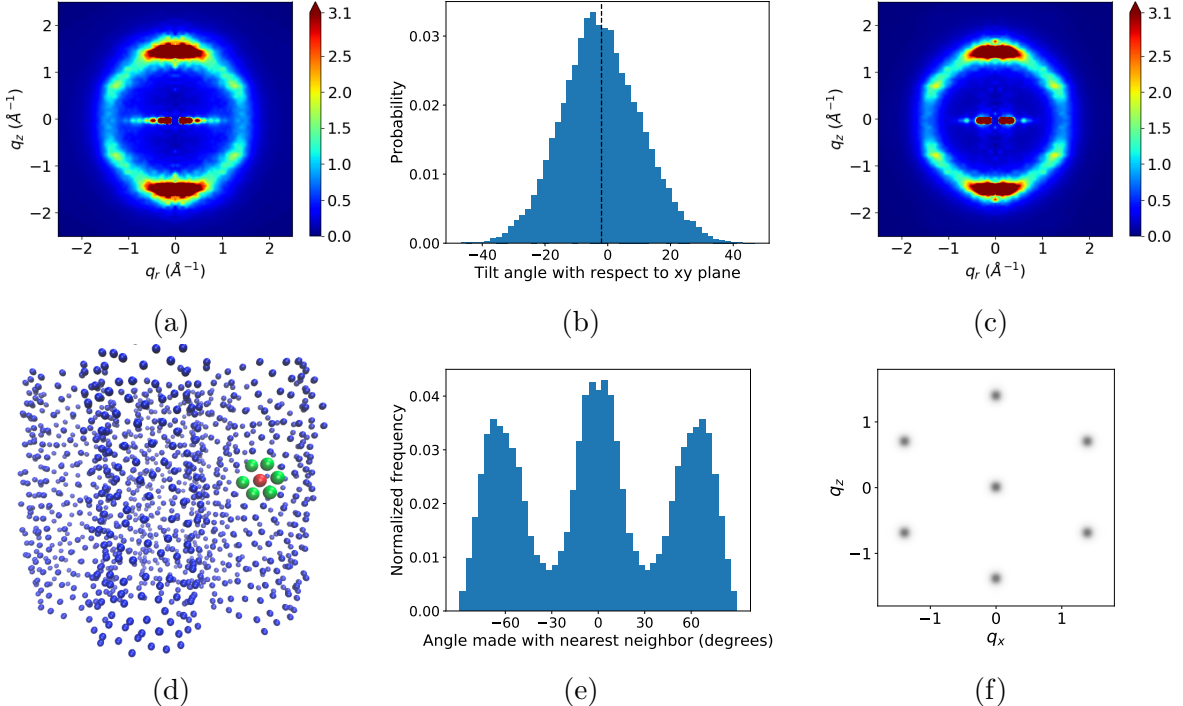


Figure 7: (a) R-spots increases in intensity when the temperature of the system is lowered to 280 K. (b) We measured the average angle made between each monomer alkane tail and the membrane plane. The average tilt angle (dashed line) is near -2° which is far from the 37° tilt angle previously used to explain R-spots. (c) To isolate the main cause of R-spots, we removed all atoms from the trajectory except for carbon atoms that constitute the tails. The simulated XRD pattern of the tails-only trajectory still shows R-spots. (d) Since the tails stay relatively flat, we plotted the center of mass of the first four carbon atoms of each tail originating from the head groups (for example, green colored centroids in the plot surround the red centroid in hexagonal fashion). Visually, the packing looks hexagonal. (e) We hypothesize that R-spots is the result of ordered tail packing. Defining the membrane plane to be 0° , we measured the angles between each COM and its nearest neighbor COMs for the equilibrated sandwiched configuration simulated at 280 K. Peaks appear in the distribution at -60° , 0° and 60° . (f) The Fourier transform of a hexagonally packed grid of points defined by the angles in (e) shows intensity at the same locations where we expect to see R-spots, as well as intensity along the q_z axis where R- π would appear.

configuration as an example. In this section, we explore the various contributions to these discrepancies, and use this information to speculate on what reasonable differences in the simulations could explain them.

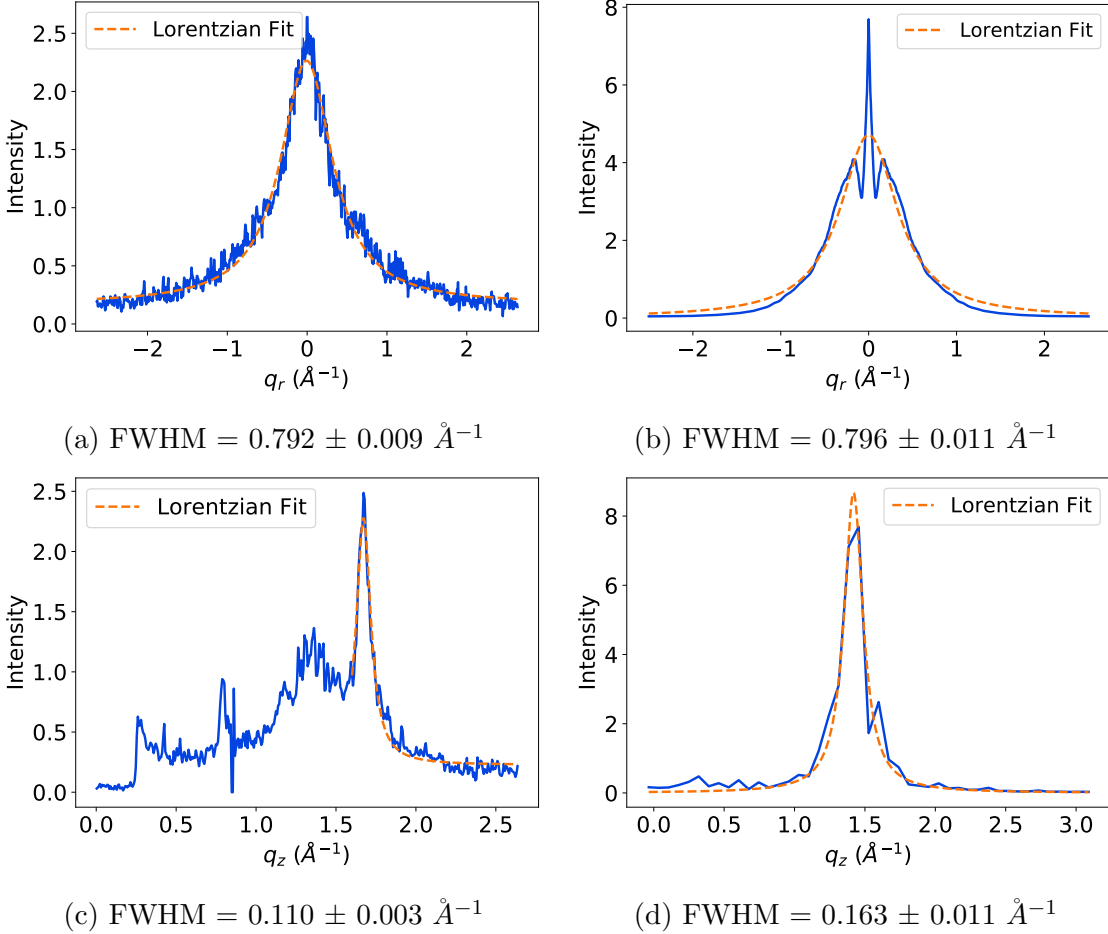


Figure 8: The maximum intensity of R- π generated from simulations of the ordered parallel displaced configuration is 3 times larger than experiment. The q_r cross-section of R- π ((a) and (b)) is qualitatively different between experiment (a) and simulation (b). We fit Lorentzian profiles to each peak and the FWHM (full width at half maximum) of the simulated pattern agrees with experiment within error. However the fit to the simulated data is affected by the three sharp peaks which appear near $q_r = 0$. The q_z cross-sections of R- π ((c) and (d)) are qualitatively similar. Each fits a Lorentzian profile well, however the FWHM of the simulated cross-section (d) is 48% larger than the experimental cross-section (c). Additionally, the peak of the simulated q_z cross-section is located at a lower q_z value than experiment.

Distance and Correlation Between Stacked Monomer Head Groups

R- π appears at a lower q_z value in our simulations versus experiment because monomers in the simulated system stack further apart than those in the experimental system (Table 2). We calculated z -direction pair distribution functions, $g(z)$, as described in Section 2.6.4. The resulting distributions are generally characterized by decaying oscillatory behavior where the average distance between peaks corresponds to the average distance between stacked monomer head groups (Figure S24). We show that the system size in the z -direction does not significantly alter $g(z)$ in Section S19 of the SI. We calculated the equilibrated vertical stacking distance, d_{equil} , between monomers using Equation 3. The distance between stacked monomers is greater than experiment by 0.5–0.9 Å across all cases, with disordered basins at the high end of that range. This behavior is not surprising since GAFF models atoms as point charges and does not appropriately model the aromatic $\pi - \pi$ interactions, which would make it more energetically favorable for the monomers to stack closer together.²⁶

The broadening of the q_z cross-section of R- π is related to z -directional correlation between scatters within monomer columns. The correlation length varies as the inverse of the full width at half maximum (FWHM) of the q_z cross-section of R- π .⁴⁷ Using this technique, we calculated the correlation length of the experimental system to be 9.0 Å. As scatterers become less correlated, we expect that R- π will broaden.

The correlation lengths of vertically stacked scatterers in our atomistic simulations are in reasonable agreement with experiment. Since it is not feasible for us to simulate membranes with much taller columns in order to obtain increased q_z resolution of our simulated XRD patterns, and because the simulated peak shape is convoluted by the extremely intense maximum of R- π , we measured correlation length by fitting Equation 2 to the peaks of $g(z)$. The correlation length of the parallel displaced, ordered basin system shows the closest agreement with experiment (Table 2). We could not extract a reliable correlation length from the disordered parallel displaced configuration since the peaks do not show clear patterns that can easily be fit to an exponential decay. The correlation length of both sandwiched

systems are relatively low because the height of the first peak of $g(z)$ is so high.

Overall, we believe our simulations exhibit a realistic amount of distance correlation in the direction parallel to the pore axis between head groups within each column. The difference in the FWHM of the q_z cross-section of R- π between experiment and simulation is less than one bin size (Figures 8c and 8d). The more significant difference between the two cross-sections is their maximum intensity which we study in more detail below.

Table 2: The correlation length is larger for systems in the ordered basin. The equilibrated vertical stacking distance, d_{equil} , is also smaller.

System	d (Å)	d_{equil} (Å)	Correlation Length (Å)
Sandwiched	3.7	4.27 ± 0.03	4.2 ± 0.8
Parallel Displaced	3.7	4.33 ± 0.04	14.5 ± 1.3
Sandwiched	5.0	4.48 ± 0.07	3.2 ± 0.9
Parallel Displaced	5.0	4.60 ± 0.08	$< d_{equil}$
Experiment	—	3.70	9 ± 1

Shape and Intensity of the q_r Cross-section of R- π

In addition to the maximum intensity of R- π being too high, the shape of its q_r cross-section in the simulated XRD is qualitatively different from experiment (Figures 8a and 8b). We attempted to fit a Lorentzian profile to the q_r cross-section and although the FWHM agrees with experiment within error, the fit is not optimal due to the three sharp peaks that appear near $q_r = 0$.

An exact quantitative comparison between the intensity and FWHM of the experimental and simulated cross-sections of R- π is not feasible for several reasons. Experimental peaks broaden due to effects that we can not easily simulate such as finite size crystalline domains and instrumental resolution.⁴⁸ In our simulated XRD patterns, the system size imposes limitations on the resolution, which makes it difficult to reliably fit peaks. This is especially problematic when comparing the FWHM of the q_z cross-section of R- π , where the experimental FWHM (0.11 \AA^{-1}) is similar to the bin size in the q_z direction (ca. 0.07 \AA^{-1}).

Additionally, we model each atom with a Gaussian sphere of electron density, which is a simplification. However, we can explore reasons for which differences in the simulation structure could change the peak shapes and intensities to be in better agreement with experiment.

We studied the shape and intensity of R- π by setting up simplified systems where we represent monomer head groups as point scatterers, as described in Section 2.7. The amount of quenched and thermal disorder present in the atomistic system, which we applied to the simplified systems, are given in Table 3. The quenched disorder, the deviation of monomers from idealized symmetric configurations, is several times greater than thermal disorder, the deviations of the monomers from their average positions during the production simulations.

Table 3: Deviation of the positions of the center of mass of head groups from their average positions (thermal disorder) as well as their idealized positions (quenched disorder) to use as simulated disorder in our model system.

System	Thermal Disorder			Quenched Disorder		
	σ_x (\AA)	σ_y (rad)	σ_z (\AA)	σ_z (\AA)	σ_θ (rad)	σ_r (\AA)
Ordered Sandwiched	0.31	0.33	0.34	1.48	0.43	2.30
Ordered Parallel Displaced	0.51	0.52	0.30	1.45	0.43	2.28
Disordered Sandwiched	0.41	0.57	0.32	1.58	0.43	2.93
Disordered Parallel Displaced	0.39	0.31	0.33	1.65	0.43	2.63

When we allow simplified monomer columns to move independently in the z -direction, the intensity of R- π drops and the q_r cross-section of the simulated diffraction patterns smooths out. We can demonstrate this by creating a simplified sandwiched configuration (as described above), with varying amounts of statistical correlation between columns (see Figure 9). In the low independent motion limit, the COM of columns are situated at the same z -coordinate. We allow increasing independence of columns by randomly shifting each column in the z -direction according to a uniform distribution bounded by $(0, f \times d)$ where f ranges between 0 and 1 and d is the vertical distance between scatterers. When $f = 1$, the columns move independently and the q_r cross-section smooths out completely (Figure 9c). Any amount of dependence results in some presence of sharp peaks, though significantly attenuated at f nearer 1. The intensity of R- π also decreases with increasing column independence. We see

an 9-fold decrease in the intensity of R- π when $f = 1$ versus when $f = 0$ for our simplified model systems.

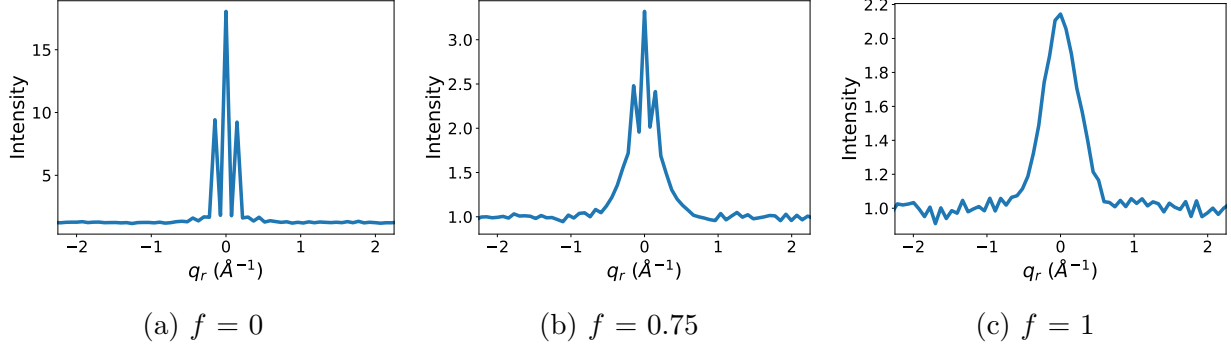


Figure 9: As we increase column independence using the f parameter, the intensity of R- π decreases and the q_r cross-section of the simulated diffraction pattern becomes more smooth. (a) When we place all columns at the same reference z coordinate, $f = 0$, the intensity of R- π is 18.3 and is characterized by sharp Bragg-like peaks. (b) When columns have a moderate amount of independence, $f = 0.75$, the intensity of R- π decreases 5-fold to 3.4. The edges of the peak are beginning to smooth out, but sharp peaks still exist. (c) When columns are completely independent, $f = 1$, the intensity of R- π decreases 9-fold to 2.1 and the cross-section is relatively smooth.

We also used our simplified systems in order to study the influence of increased disorder in each dimension. Increasing z -directional disorder reduces the intensity of R- π without changing the shape of its q_r cross-section. Increasing disorder on the xy plane, somewhat counterintuitively, reduces the FWHM of the q_r cross-section of R- π with an insignificant effect on its intensity. We explain these points in more depth in Section S20.

Quenched Disorder in Ensembles of Configurations

Since the dynamics of this system are slow, consequently most of our analysis has been focused on a set of quenched configurations with some structural characteristics that do not vary significantly with time. We therefore attempted to learn more about their time-averaged structures by studying ensembles of shorter simulations started from more independent initial configurations. To do this, we created ensembles of 40 simulations in both the parallel displaced and sandwiched configurations. We used the same equilibration scheme described

in Section 2.5. However, we built the initial configurations with columns randomly displaced in the z -direction and looked at the results after 5 ns of unrestrained simulation, which should capture any quenched disorder built in from the initial configurations. We then simulated XRD patterns from the 40 trajectories, concatenated together. The q_r cross-sections of R- π generated from the two concatenated trajectories are shown in Figure 10.

Qualitatively, the q_r cross-sections of R- π generated from ensembles of simulations are nearly smooth, with only small spikes near $q_r=0$. These data suggest that the average intensity of R- π in the ensemble of sandwiched systems is about 3× higher than that in the ensemble of parallel displaced configurations. Compared to our long simulations, the intensity of R- π generated from ensembles of short simulations decreases by a factor of 3 and by a factor of 2 for the sandwiched and parallel displaced configurations respectively.

Overall, the intensity of R- π generated from the parallel displaced ensemble of short simulations shows the best agreement with experiment so far. For simplicity, we will limit the following discussion to the parallel displaced configuration. Data for the sandwiched configuration is presented in Section S21.

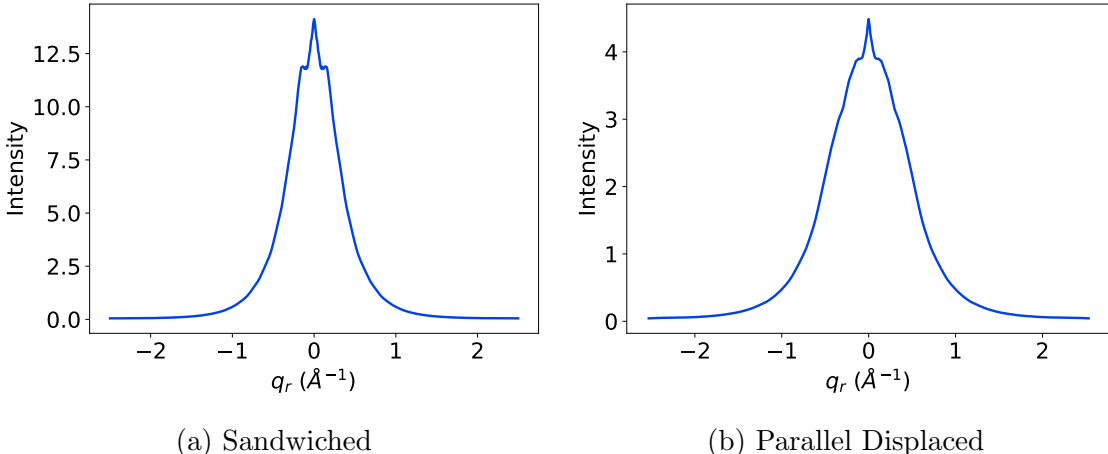
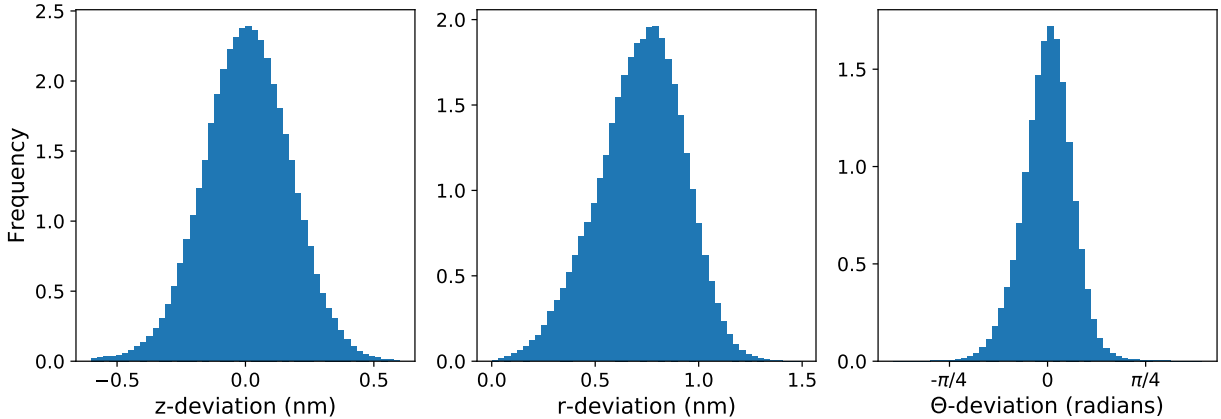


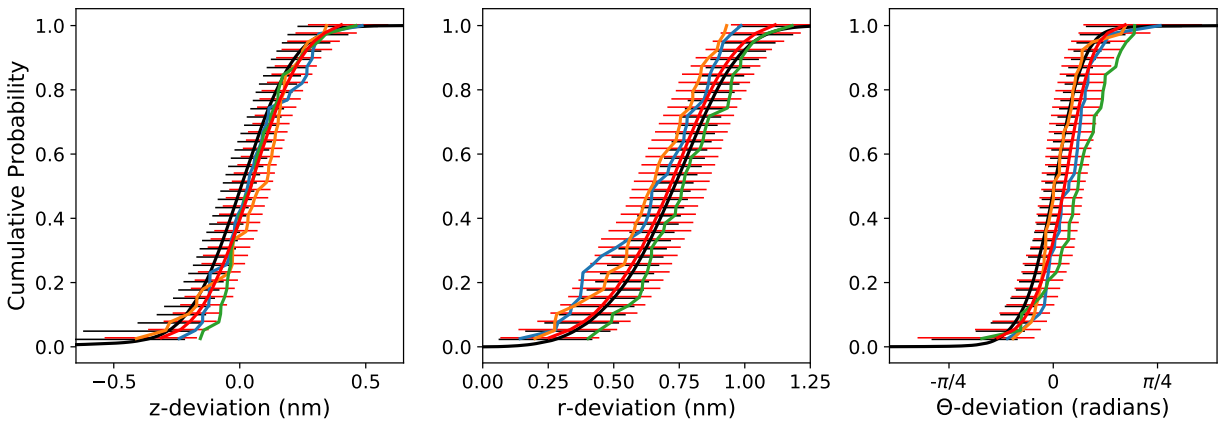
Figure 10: The q_r section of R- π is much smoother than Figure 8b when we generate simulated XRD patterns from an ensemble of 40 independent simulations, suggesting that much of the extra initial intensity may be due to the starting conditions. The maximum intensity of R- π is 3× higher in the sandwiched configuration (a) than in the parallel displaced configuration (b).

These short independent simulations exhibit a symmetric distribution of quenched disorder providing evidence that the quenched disorder is randomized in each system. The only difference between each independent initial configuration is the random z -direction displacement that we apply to each column. The quenched disorder is then a result of the initial structural collapse that is directed by the randomized velocity vectors of the system's atoms drawn from a Maxwell-Boltzmann distribution. We pooled the deviations of each head group COM from idealized positions from all independent simulations in order to create the distributions shown in Figure 11a (see Section 2.7). The distributions appear symmetric meaning that there is an equal chance for a head group to displace in the positive or negative z , r , or θ -direction.

We verified that this same symmetry exists for individual COMs. If we consider the COM of a given head group, we expect that the distribution of its deviations from its idealized position among all the independent simulations should be symmetric about its idealized position. We can calculate the empirical cumulative distribution function (ECDF) of these distributions of deviations. The ECDFs of 3 randomly selected COMs are shown in Figure 11b to guide the eye (colored lines). The average of all COM ECDFs is represented by the red line with the 95% confidence interval represented by the red error bars. We also calculated the ECDF from the full distributions in Figure 11a (black line with error bars). We generated error bars that represent the 95% confidence intervals by performing 1000 trials where we randomly sampled 40 values (the same as the number of independent simulations) from the distributions in Figure 11a, then measured the deviation between the sampled ECDF and the full ECDF. These error bars are generally smaller than those generated from the 400 COM ECDFs, as there is a wider distribution of mean COM deviations than the mean deviations from distributions sampled from the full distribution. The similarity between entirely independently sampled ECDFs and the ECDFs from individual independent simulations supports the hypothesis that each quenched configuration is random and mostly independent.



(a) Distributions of deviations from ideal positions generated with data from all independent simulations



(b) Empirical cumulative distribution functions generated from (a) and from simulation ensembles.

Figure 11: (a) The distributions of the head group COM deviations from their idealized positions generated using pooled data from all frames of each independent configuration are symmetric, implying that there is equal probability for a head group to displace in the positive or negative z , r or θ -direction. (b) The COM position of a given head group is displaced randomly upon quenching. The ECDF generated from the pooled distributions (black) in (a) agree with the means of the ECDFs generated from each COM (red). The red error bars are larger than the black error bars since there is a wider distribution of mean COM deviations than the mean deviations of distributions sampled from the full distribution.

The systems that we simulated for 400 ns and then used for most of our analysis are representative of the long term simulation behavior of any system chosen from the ensemble. The distributions of standard deviations generated from each of the ensemble trajectories (Figures 12a and 12b) are fairly tight with $(\sigma_{\sigma_z}, \sigma_{\sigma_r}, \sigma_{\sigma_\theta}) = (0.011 \text{ nm}, 0.007 \text{ nm}, 0.022 \text{ radians})$. We analyzed the first 5 ns of the 400 ns ordered parallel displaced configuration

and observed the same amount of disorder (based on the σ values in Figure 12a) with indistinguishable mean values. Additionally, we calculated the radial density of monomer components as a function of their distance from the pore centers (Figure 12c). All simulations have similar profiles. The distribution of sodium ions near the pore center is relatively noisy since the sodium ions have much more translational freedom than the head groups.

The Implications of the New-found Understanding of R- π

We can explain the discrepancies between R- π seen experimentally and in simulation using what we have shown in this section. The stacking distance between monomer head groups is too large, likely due to failures of the force field to appropriately model $\pi - \pi$ interactions. The intensity of the simulated R- π is too high, which may be a consequence of too much short-range ordering in the z -direction in addition to high degrees of correlation between columns. Finally, the q_r cross-section of R- π is not smooth, which is also likely a consequence of columns that are too highly correlated. If we limit ourselves to standard simulation techniques, it is necessary to average data generated from ensembles of independent simulation trajectories in order to begin converging on time-averaged descriptions of the system's molecular structure.

A secondary conclusion drawn from the evidence in this section is that the architecture of each column is likely in between our sandwiched and parallel displaced configurations. The parallel displaced configuration that we have simulated in this paper is an exaggerated manifestation of the parallel displaced $\pi - \pi$ stacking mode. Not only is the intensity of R- π calculated from the ensemble of parallel displaced simulations in close agreement with experiment, but the experimental WAXS pattern shows faint off-axis features at the same q_r value as R-double which are only present in simulated patterns generated from parallel displaced configurations. The monomers may prefer to be parallel displaced, but their displacement is likely only slightly shifted, on the xy plane, from the center of mass of their vertically adjacent neighbors (see Figure S10 of the SI). In this way, columns can more easily act independently while maintaining some features of parallel displaced structure.

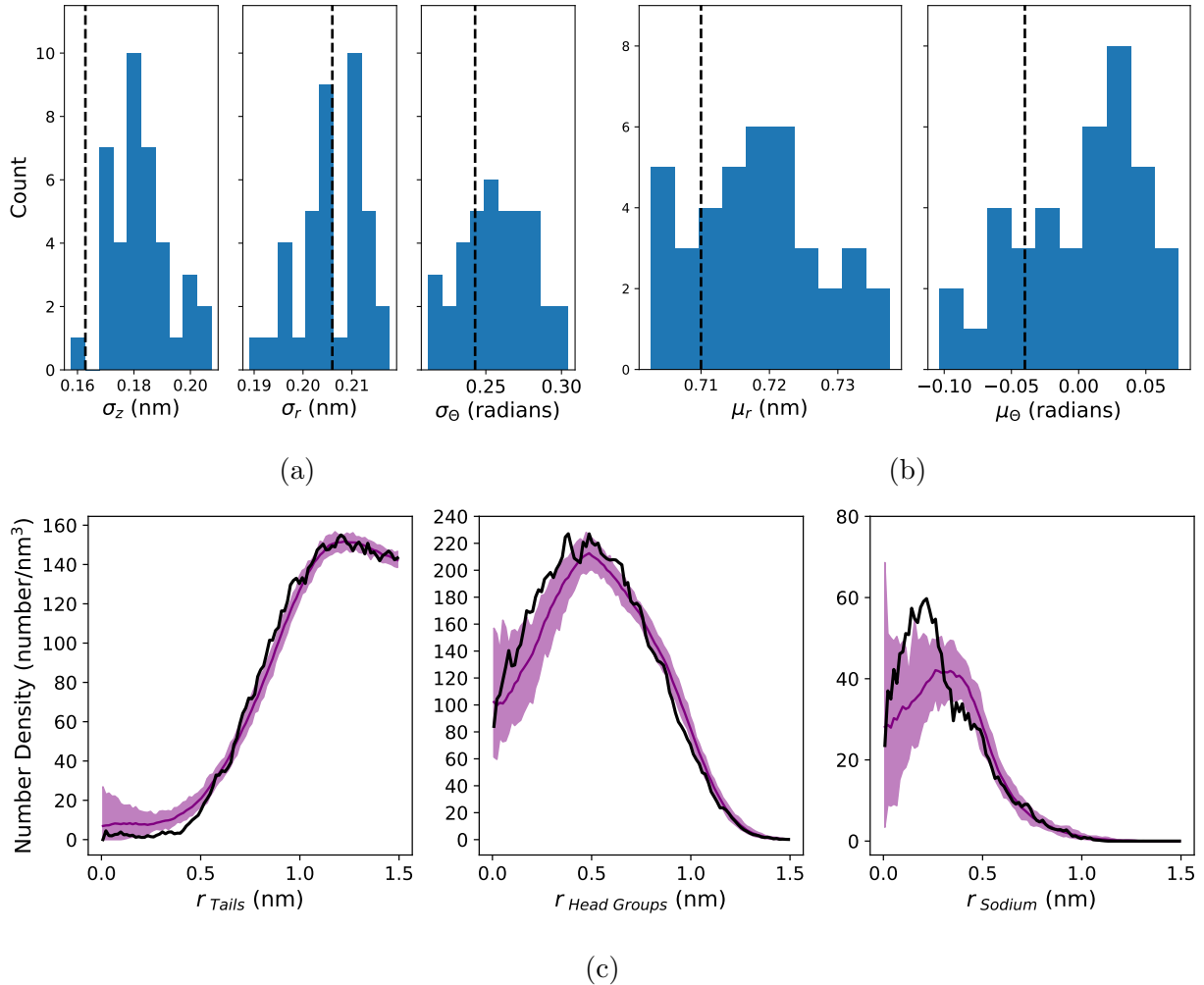


Figure 12: (a) The standard deviation of the distribution of quenched disorder from the first 5 ns of the main ordered parallel displaced system studied in this paper (black dashed line) is in agreement with the distribution of quenched disorder standard deviations calculated from the ensemble of simulations (histogram). (b) The mean values of r and θ from the first 5 ns of the main system trajectory (black dashed line) is in agreement with the distribution of mean values calculated from each simulation in the ensemble (histogram). The mean values of z are necessarily 0 so they are not plotted. (c) The radial densities of tail atoms, head group atoms and sodium atoms calculated from the first 5 ns of the main system simulation trajectory (black lines) and from the ensemble of trajectories (all other lines) look qualitatively similar.

3.2.5 Origin of R-double

R-double does not appear in any of the simulated diffraction patterns generated using the systems simulated up to this point. Here we hypothesize several configurational arrangements which may lead to the appearance of R-double and show that we cannot achieve a long-term

stable system that exhibits R-double without the inclusion of small amounts of water in the pores.

The appearance of R-double implies a vertical modulation in electron density every 7.4 Å. We are not able to achieve such modulation using our simple initial configurations. Although the position of monomers in parallel displaced configurations alternate every other layer, such a configuration will not produce R-double, but only off-axis reflections at the same q_z value.⁴⁹ There is not a unique solution that describes the origin of R-double. Extracting the exact relationship between a diffraction pattern and its real space configuration is well-known as the phase problem.⁵⁰ We have proposed configurations that result in the appearance of R-double below, and we can speculate which makes the most physical sense.

One way to produce R-double is if our initial configuration contains alternating parallel and anti-parallel carboxylate groups relative to the plane of the monomer's phenyl ring. It is difficult to physically justify this system. Systems built this way are only stable if position restraints are placed on all head group heavy atoms. Carboxylate groups quickly revert to the parallel position as restraints are released. There is an appreciable energy barrier that prevents rotation of carboxylate groups attached to phenyl rings since the group extends the system's π conjugation⁵¹ (see Figure S30 of the SI), which is significant even considering possible overestimates of the barrier height in the classical force field.

Another way to produce R-double is if we rotate monomers with respect to vertically adjacent monomers. In this configuration, the LLC monomers are rotated so that the vector created by the bond extending from the carboxylate carbon to the phenyl ring is oriented $\pm 15^\circ$ with respect to the vector extending from the head group COM to the pore center (Figure 13a). Every other monomer layer is rotated $+15^\circ$ and those in between are rotated -15° . This configuration allows monomer tails to sit between adjacent monomer tails which may be the most favorable way for them to pack. This configuration is only stable for a few nanoseconds and R-double quickly fades.

We can also produce R-double if the LLC monomers are not uniformly spaced in the

z -direction, but instead are placed in pairs that stack less than 3.7 Å apart, with COMs that are spaced 7.4 Å from neighboring pairs of monomers (Figure 13b). Simulations of unevenly spaced systems are only stable while position restraints are applied to heavy atoms of the phenyl rings. There is little evidence from quantum mechanical studies of stacked $\pi - \pi$ systems that such uneven stacking could be energetically stable.⁵² As soon as we remove position restraints, our system tends towards uniformly spaced monomers.

The addition of water to the system promotes the appearance of R-double, providing an answer to Question 3 posed in the introduction. We added water to the parallel displaced and sandwiched configurations in the ordered basin and equilibrated them according to the wet equilibration procedure. There is no experimental measurement of water concentration in these membranes so we tested a range of water concentrations from 1% to 5%. R-double appears transiently in the simulated XRD pattern of the parallel displaced configuration with 1 wt% water (Figure 13c). It is not initially present, but appears after 200 ns of simulation time. After 450 ns, it disappears again. Simulated XRD patterns of all other solvated systems tested are shown in Figure S31, however R-double is not present.

R-double appears in the solvated system due to the structuring of the head groups. To demonstrate this, we removed the head groups from the trajectory used to produce Figure 13c in order to produce that shown in Figure 14a. R-double does not appear without the presence of the head groups. Water molecules must therefore play a role in the structuring of the head groups in these simulations since R-double does not appear in any dry simulations.

The addition of a small amount of water to the pores stabilizes non-uniform stacking of head groups much like that shown in Figure 13b. When two vertically stacked monomer head groups hydrogen bond with a shared water molecule, the monomers are drawn closer together (as illustrated in Figure 14b), which creates the asymmetry that allows R-double to appear. If a monomer head group shares a hydrogen-bonded water molecule with a head group above itself, it will be less likely to share a water molecule with a head group below it due to geometric constraints. The monomer head group below can just as easily share a

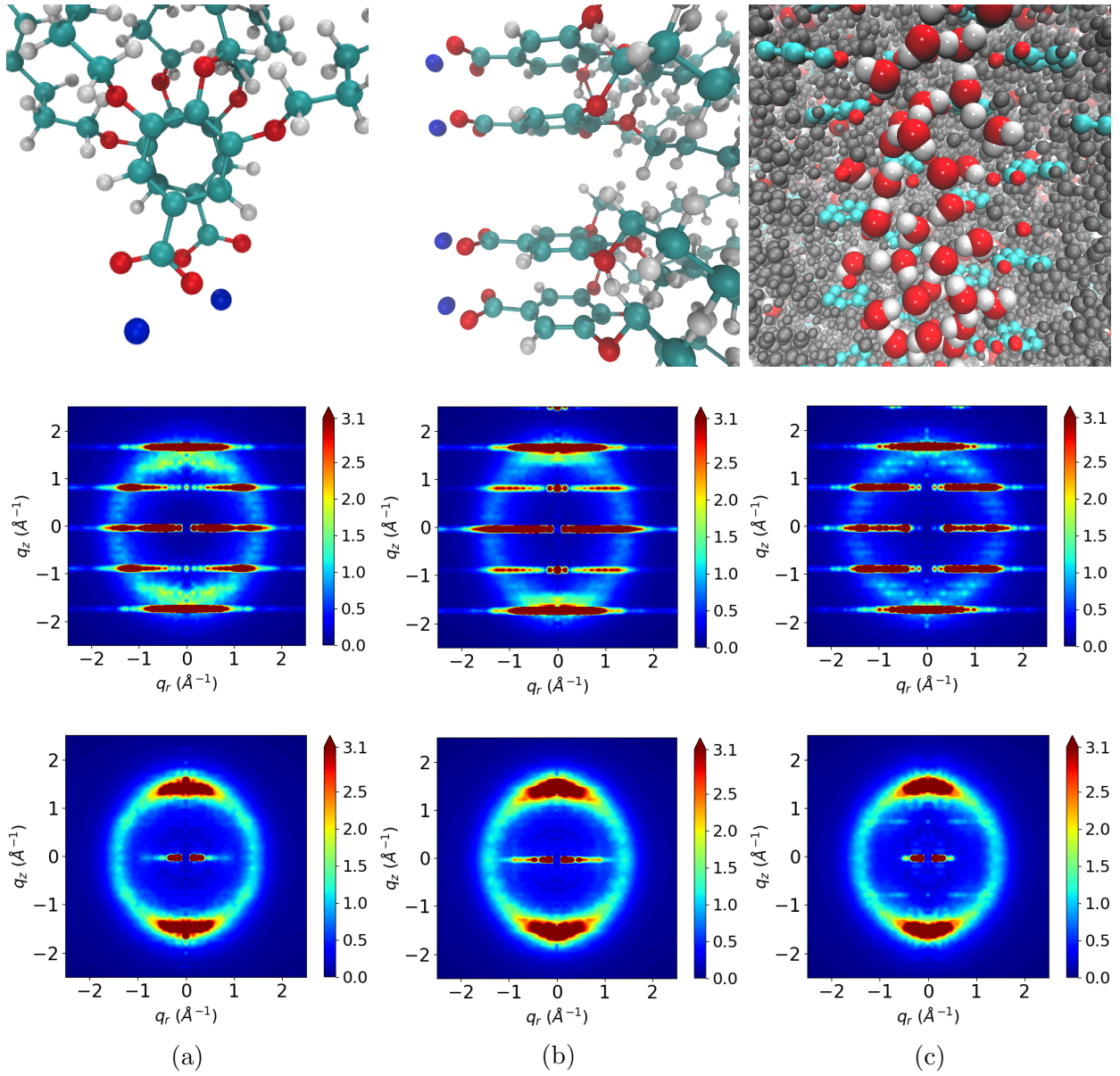


Figure 13: (a) When monomer head groups are rotated with respect to vertically adjacent monomers (top), R-double is visible while the heavy atoms of the head groups are held in place with position restraints (middle). R-double fades once the position restraints are released. (b) When monomers are non-uniformly spaced (top), R-double appears if all heavy atoms of the head groups are held in place with position restraints (middle). R-double quickly fades once the position restraints are released (bottom). (c) When we add 1 wt% water to the parallel displaced configuration in the ordered basin (top) R-double is not initially present during the restrained portion of equilibration (middle). After 200 ns of equilibration, R-double becomes visible and persists for another 200 ns (bottom).

water molecule with a head group below itself. There are a modest number of occurrences of this scenario, which we quantify in further detail in the SI, Section S24.

Of all the configurations tested, it is most likely that R-double is induced by water molecules as described above since it is the only mechanism that can be observed without position restraints. The extent of the hydrogen-bonded network that forms is largely determined by the accuracy of the forcefield. It is possible that a more realistic force field would make the effect stronger or weaker. If this is truly the mechanism, it implies that the system studied by Feng et al.^{16,19} was not truly a thermotropic Col_h phase. Rather, they were very low water content H_{II} phases unintentionally created due to the neat monomers' hydroscopicity. Anecdotal evidence from other researchers suggests that membranes are less likely to assemble under completely dry conditions, supporting the idea that the “dry” structures do absorb some water. This detail may therefore be important for reproducing the results of Feng et al.

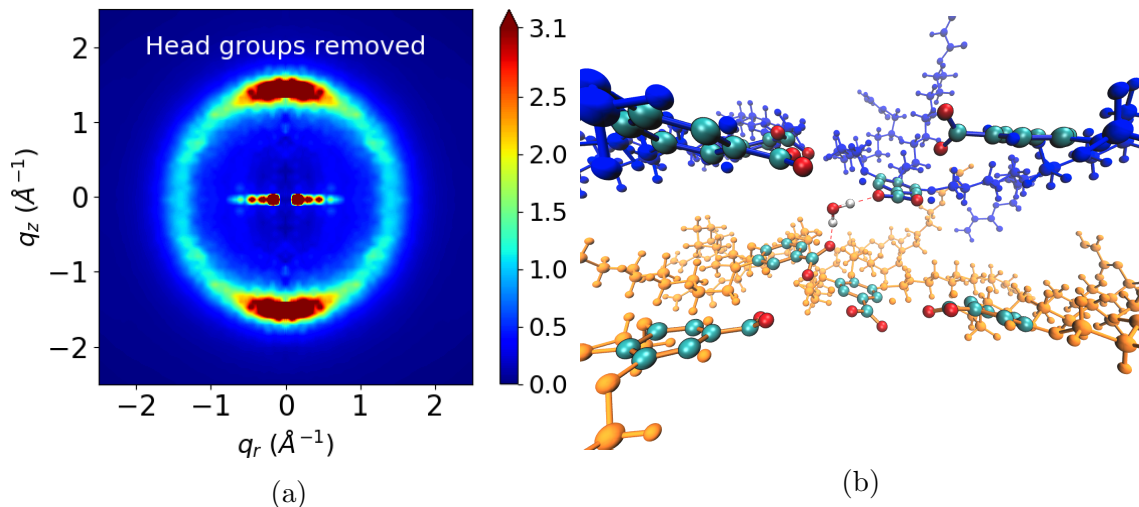


Figure 14: (a) The structure of the head groups is responsible for the appearance of R-double. When we remove head groups from the trajectory, the simulated diffraction pattern no longer shows R-double. (b) Monomer head groups above or below each other that hydrogen bond with a shared water molecule are drawn closer together in the z -direction. Blue monomers were stacked above orange monomers in the initial configuration.

3.3 Atomistic Structure of the Pore Columns

We are most interested in the structure and composition of the pores since we would like to study transport mechanisms within them. We have shown that the tails possess a certain

degree of order which is necessary in order to create the complex WAXS pattern shown experimentally, but they will not be involved in a separation process. We aim to further understand the pore architecture, in order to address Question 4 posed in the Introduction, and observe the differences, if any, between the different plausible equilibrated configurations studied so far. In general, the composition of each region, particularly within our definition of the pore region, is similar between all systems.

We plotted the number densities of heavy atoms in the head group (Figure 15a), carbon atoms in the tail region (Figure 15b) and all sodium ions (Figure 15c). For the head group region, we used heavy atoms making up the aromatic rings and carboxylate groups. For the tail region, we used carbon atoms of the monomer tails (See Figure S13 of the SI for a diagram). We averaged the histograms over the equilibrated portion of the trajectory. There is a gradient in pore composition transitioning radially from the hydrophilic to the hydrophobic region, rather than an abrupt division. Based on size-exclusion experiments, the pore radius was estimated to be 0.6 nm.¹¹ However, the simulations do not confine sodium ions and head groups to just within this experimentally-defined pore region. For dry systems, 19% of sodium ions exist outside the pore region (except sandwiched, ordered basin, where 16% are outside the pore). Additionally, in all cases, about 3% of the plotted tail density is located within the pore region (except ordered sandwiched, where 1.5% are within the pore region). For the solvated system, the results are similar, however the head group density is shifted slightly radially outward, due to swelling of the pore by water.

The space in the pore region is filled with a mixture of sodium ions and head groups. The distributions appear somewhat different near $r=0$, but noise is higher since there is significantly less sampling as r approaches 0. Regardless, all systems, including the solvated system, have a significant number of head groups and sodium ions occupying the pore center. This observation highlights that the pore region is dense, not hollow, and may impede transport of solvent and solutes when compared to the previous idealized picture of a hollow tube conducive to transport.

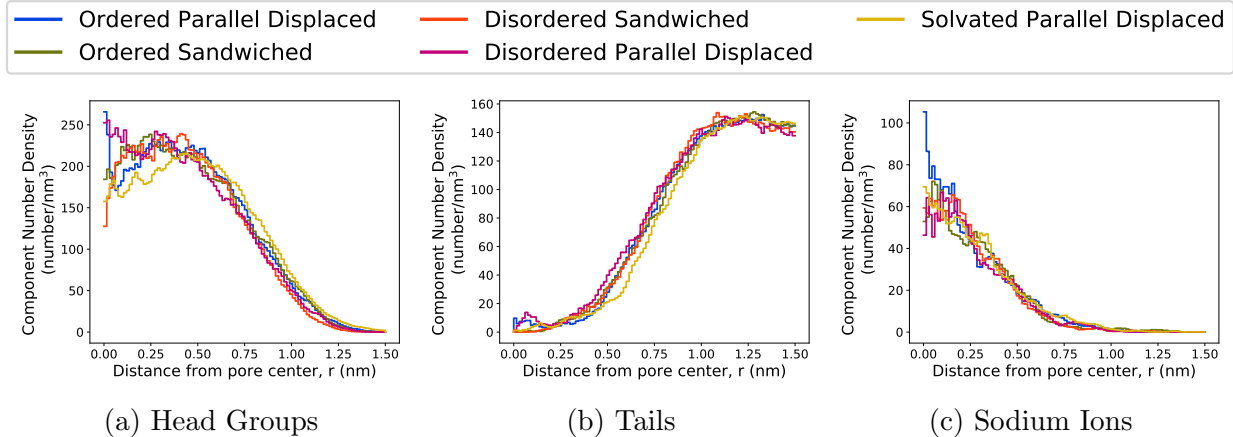


Figure 15: In all cases, the component radial distribution functions are similar. They exhibit a composition gradient transitioning from the hydrophilic to the hydrophobic regions. The biggest differences are at $r=0$ where noise is higher due to decreased sampling. The center of the pore is not hollow, but contains sodium ions and head groups, even when the system is solvated. This architecture may impede transport in the real system in a chemically-dependent manner. The solvated system has a lower density of head groups near the pore center which is likely due to the swelling that is necessary in order to fit water molecules in the pore region.

Our observations suggest that the details of transport may be relatively independent of the structural differences between different possible structures studied here. Despite the structural intricacies that give rise to differences between the various metastable basins, all pores are characterized by dense, primarily hydrophilic cores with a gradient towards a primarily hydrophobic tail region far from the pore center. This implies that we might see the same trends in transport properties from any of the systems studied so far. Since the ultimate goal of our work is to design new monomers using high throughput simulations, achieving that goal becomes tractable without the need to optimize every system with an experimental dataset.

3.4 Slow Dynamics

We observe slow dynamics in our system. Typical diffusion constants for columnar liquid crystals have been reported to be between 10^{-11} m²/s⁵³ and 10^{-14} m²/s.⁵⁴ In the case of

LLCs, we would expect a diffusion coefficient at the low end of this range since hydrophilic regions of monomers can hydrogen bond, thus increasing the energetic barriers for motion. We measured the diffusion constants of monomers in each of the main systems we studied (see Table S4 of the SI) and find they are all on the order of 10^{-14} m²/s. However, since on this timescale, no monomers move a full ‘level’ above or below, this may be an overestimate. This slow speed is not entirely surprising considering how densely the monomers are packed as implied by diffraction experiments. The entangled tails likely restrict both vertical and lateral movement.

Consequently, there is not enough movement on the timescales we simulated for the system to consistently reach a definitive equilibrium structure. In all cases our monomers equilibrate to a stacking distance that is too large compared to experiment. As discussed in Section 3.2.4, while this may be in large part due to the force field’s inability to model aromatic interactions, it is also possible that the monomer tails do have enough time to pack as tightly as they could. More densely packed tails could allow the monomers to stack closer together.

We quantified the movement of the tails during our simulations by calculating the autocorrelation function of the dihedral angle formed around the bond between the head groups and the ether oxygens which attach the tails to the head group (see Figure S35 of the SI). We exclude the dihedral from the middle tail since it is fundamentally different than the two symmetric outside tails. We limited these studies to the sandwiched configuration for simplicity.

The ether dihedrals become decorrelated on a reasonable timescale when we raise the system temperature. At 300 K (Figure S35a), the autocorrelation function does not cross the *x*-axis until \sim 105 ns meaning that tails fully rotate on average about 4 times over the course of the 400 ns that we studied. Additionally, the correlation function plateau’s near a value of -0.2 which indicates that the tails are starting in an unfavorable configuration. We implemented distance restraints between the centers of mass of monomer head groups to

preserve the hexagonal phase, then raised the temperature of the equilibrated 300 K ordered basin sandwiched system to 500 K. We witnessed decorrelation of the ether dihedrals after \sim 11 ns with a plateau at 0, (Figure S35b) indicating a complete loss of memory. We annealed the resultant configuration back down to 300 K over 200 ns to see if the increased rotational freedom might allow the system to relax into to a more tightly packed configuration.

Decorrelating the ether dihedrals at high temperature, followed by thermal annealing does not improve packing in our model. In the ideal case, if all monomers stacked 3.7 Å apart, the *z*-dimension of our unit cell should be 7.4 nm. In the ordered basin, sandwiched system studied in this paper, the *z*-dimension of the unit cell equilibrated to 8.87 nm, which is roughly consistent with the stacking distance reported in Table 2. After 200 ns of annealing from 500 K to 300 K, the *z*-dimension of the unit cell was 9.22 nm. We repeated the annealing procedure over the course of 400 ns and the final *z*-dimension of the unit cell was 9.20 nm. Much longer annealing simulations may get the system to the correct density, but such simulations are beyond the scope of the current study.

3.5 Ionic Conductivity Measurements

We calculated the ionic conductivity of the parallel displaced configuration in the ordered basin with 1 wt% water since we believe its structure is the closest match to experiment. Our model estimates the ionic conductivity to be $(5.92 \pm 0.05) \times 10^{-5}$ S/m, about 5 times higher than the experimental value of $(1.3 \pm 0.1) \times 10^{-5}$ S/m. We verified the value calculated by the Nernst-Einstein relationship using the collective diffusion model⁵⁵ (see Section S15 of the SI). The values calculated by the collective diffusion model agree with Nernst-Einstein values within error, however there is a much higher uncertainty that would require much longer simulations to lower.

The calculated value of ionic conductivity is 5 times higher than experiment likely because we simulated infinitely long, aligned pores and because our model over-predicts the diffusivity of sodium. The ionic conductivity measurement to which we are comparing was done with

an 80 μm -thick film, nearly 10,000 times thicker than our simulated system. The thick film is likely imperfectly aligned and has defects leading to non-contiguous pores. It has been shown that there is a large dependence of ionic conductivity on the alignment of the pores. The ionic conductivity of an isotropically aligned film is ca. 85 times lower than that of the nearly aligned film to which we are comparing.¹⁶ Additionally, sodium ions parameterized with AMBER parameters exhibit bulk water diffusion coefficients that are two times greater than experiment.⁵⁶ We cannot definitively say how this ratio changes in the confined LLC pore environment, but it is likely that sodium diffuses faster than experiment in our system which contributes to a higher ionic conductivity.

3.6 Effect of Cross-linking

Experimentally, membranes are cross-linked for mechanical stability before use. We applied our cross-linking algorithm to equilibrated sandwiched and parallel displaced configurations in the ordered pore basin. We allowed the cross-linking algorithm to propagate until greater than 90% of the vinyl groups on the tails of the monomers were either involved in a cross-linking reaction or were terminated (see Section S13 of the SI for further details of the cross-linking algorithm). We allowed the cross-linked configurations to simulate for 100 ns further in the NPT ensemble.

There are only minor changes to the physical characteristics of these systems when they are cross-linked (See Figure S36). The ionic conductivity of the sandwiched configuration decreases while that of the parallel displaced configuration stays the same. The pore spacing decreases in both systems by 0.07 nm. The vertical monomer stacking distance increases in the sandwiched configuration and decreases in the parallel displaced configuration, however the values of cross-linked configurations fall within uncertainty of their un-cross-linked counterparts. The correlation length decreases in both systems, but is most pronounced in the parallel displaced system.

4 Conclusions

We have used detailed molecular modeling of the Col_h phase formed by Na-GA3C11 in order to study its nanoscopic structure. While there have been efforts to model formation of various liquid crystalline phases with molecular dynamics, to our knowledge there have been no studies which attempt to examine their structure with the same level of detail presented here.

We observed a number of metastable configurations, stable for hundreds of nanoseconds, which do not fit the experimental profile we have tried to match. We explored two classes of metastable basins which are dependent on the initial vertical stacking distance between monomers: the ordered and disordered pore basins. We expect that these metastable configurations will eventually rearrange and converge to a single equilibrium structure. We conducted extensive analysis in order to isolate structures which most closely resemble the true equilibrium structure.

We achieve maximum structural consistency with experiment, as determined by simulated 2D-XRD patterns, when we build our model in the ordered basin parallel displaced configuration with 5 monomer columns per pore and 1 wt% water. R-alkanes and R-pores appear where expected for the reasons originally predicted. We find that R-spots is likely due to ordered alkane chain packing. R- π appears at lower q_z values than experiment because monomer stack too far apart, and its intensity is far too high, likely because our initial configurations contain a high level of dependence between monomer columns. We can learn more about the time averaged structure of these systems by studying ensembles of independent simulations. Finally, we observed that our model can only produce R-double when we add small amounts of water to the system. This observation has possible implications for the reproducibility of the experimental results of Feng et al.^{16,19} since they specify that their membrane is synthesized dry.

Although exactly reproducing the experimental 2D-WAXS pattern required attention to minute structural details, we found that all systems showed similar radial distribution

functions characterized by a gradual radial transition from a dense hydrophilic core to hydrophobic tails. This observation enables us to study new systems that have not been experimentally characterized with the expectation that any additional structural optimization will not greatly influence trends in transport property predictions. The compositional gradient itself raises questions about the nature of size-exclusion separations in systems without well-defined pore boundaries, which potentially could enable separations that vary with chemical identity as well as size.

Our system can reasonably estimate ionic conductivity. Our calculations are about 1 order of magnitude higher than experiment, however that is to be expected since we are simulating a perfectly straight and defect-free membrane.

Finally, we verified that our conclusions do not change when the system is cross-linked by the algorithm we implemented. The ionic conductivity drops by a factor of \sim 1.5, in closer agreement with experiment, the pore spacing decreases and the membrane becomes thicker; however, all changes are relatively minor, preserving most of the features well.

Future work, based on what has been learned in this study, may help further improve the structural agreement between experiment and simulation and test the sensitivity of our current conclusions to a more accurate structure. Polarizable force fields such as AMOEBA which explicitly including $\pi - \pi$ interactions between aromatic functional groups may be able to draw stacked monomers closer together.⁵⁷⁻⁵⁹ We can study ensembles of long simulations in order to observe more averaged structure and to create more experimentally consistent XRD patterns. Extremely long simulations (on the order of μ s) may be necessary to better quantify the time scales for large scale rearrangements, and the precise arrangements themselves.

With the structural understanding gained by these simulations, it will be possible to evaluate transport of various solutes within the system, and apply the knowledge gained from this study in order to suggest improvements to the existing system, as well as to evaluate new unsynthesized LLC systems.

Supporting Information

Detailed explanations and expansions upon the results and procedures mentioned in the main text are described in the Supporting Information. This information is available free of charge via the Internet at <http://pubs.acs.org>.

Acknowledgements

J. Y. and M. A. G. were supported by the Soft Materials Research Center under NSF MRSEC Grant DMR-1420736

Molecular simulations were performed using the Extreme Science and Engineering Discovery Environment (XSEDE), which is supported by National Science Foundation grant number ACI-1548562. Specifically, it used the Bridges system, which is supported by NSF award number ACI-1445606, at the Pittsburgh Supercomputing Center (PSC). This work also utilized the RMACC Summit supercomputer, which is supported by the National Science Foundation (awards ACI-1532235 and ACI-1532236), the University of Colorado Boulder, and Colorado State University. The Summit supercomputer is a joint effort of the University of Colorado Boulder and Colorado State University.

The authors thank Richard Noble, Michael McGrath, Gregory Dwulet and Sarah Dischinger for useful discussions that enhanced our understanding of these LC membrane systems.

References

- (1) Fritzmann, C.; Lwenberg, J.; Wintgens, T.; Melin, T. State-of-the-Art of Reverse Osmosis Desalination. *Desalination* **2007**, *216*, 1–76.
- (2) Schwarzenbach, R. P.; Escher, B. I.; Fenner, K.; Hofstetter, T. B.; Johnson, C. A.; Gunten, U. v.; Wehrli, B. The Challenge of Micropollutants in Aquatic Systems. *Science* **2006**, *313*, 1072–1077.
- (3) Werber, J. R.; Osuji, C. O.; Elimelech, M. Materials for Next-Generation Desalination and Water Purification Membranes. *Nat. Rev. Mater.* **2016**, *1*, 16018.
- (4) Dischinger, S. M.; Rosenblum, J.; Noble, R. D.; Gin, D. L.; Linden, K. G. Application of a Lyotropic Liquid Crystal Nanofiltration Membrane for Hydraulic Fracturing Flowback Water: Selectivity and Implications for Treatment. *J. Membr. Sci.* **2017**, *543*, 319–327.
- (5) Van Der Bruggen, B.; Vandecasteele, C.; Van Gestel, T.; Doyen, W.; Leysen, R. A Review of Pressure-Driven Membrane Processes in Wastewater Treatment and Drinking Water Production. *Environ. Prog.* **2003**, *22*, 46–56.
- (6) Humplik, T.; Lee, J.; OHern, S. C.; Fellman, B. A.; Baig, M. A.; Hassan, S. F.; Atieh, M. A.; Rahman, F.; Laoui, T.; Karnik, R. et al. Nanostructured Materials for Water Desalination. *Nanotechnology* **2011**, *22*, 292001.
- (7) Cohen-Tanugi, D.; Lin, L.-C.; Grossman, J. Multilayer Nanoporous Graphene Membranes for Water Desalination. *Nano Lett.* **2016**, *16*, 1027–1033.
- (8) Hata, K.; Futaba, D. N.; Mizuno, K.; Namai, T.; Yumura, M.; Iijima, S. Water-Assisted Highly Efficient Synthesis of Impurity-Free Single-Walled Carbon Nanotubes. *Science* **2004**, *306*, 1362–1364.
- (9) Maruyama, S.; Einarsson, E.; Murakami, Y.; Edamura, T. Growth Process of Vertically Aligned Single-Walled Carbon Nanotubes. *Chem. Phys. Lett.* **2005**, *403*, 320–323.

- (10) Smith, R. C.; Fischer, W. M.; Gin, D. L. Ordered Poly(p-phenylenevinylene) Matrix Nanocomposites via Lyotropic Liquid-Crystalline Monomers. *J. Am. Chem. Soc.* **1997**, *119*, 4092–4093.
- (11) Zhou, M.; Kidd, T. J.; Noble, R. D.; Gin, D. L. Supported Lyotropic Liquid-Crystal Polymer Membranes: Promising Materials for Molecular-Size-Selective Aqueous Nanofiltration. *Adv. Mater.* **2005**, *17*, 1850–1853.
- (12) Donnan, F. G. Theory of Membrane Equilibria and Membrane Potentials in the Presence of Non-Dialysing Electrolytes. a Contribution to Physical-Chemical Physiology. *J. Membr. Sci.* **1995**, *100*, 45–55.
- (13) Hatakeyama, E. S.; Gabriel, C. J.; Wiesnauer, B. R.; Lohr, J. L.; Zhou, M.; Noble, R. D.; Gin, D. L. Water Filtration Performance of a Lyotropic Liquid Crystal Polymer Membrane with Uniform, Sub-1-Nm Pores. *J. Membr. Sci.* **2011**, *366*, 62–72.
- (14) Hatakeyama, E. S.; Wiesnauer, B. R.; Gabriel, C. J.; Noble, R. D.; Gin, D. L. Nanoporous, Bicontinuous Cubic Lyotropic Liquid Crystal Networks via Polymerizable Gemini Ammonium Surfactants. *Chem. Mater.* **2010**, *22*, 4525–4527.
- (15) Carter, B. M.; Wiesnauer, B. R.; Hatakeyama, E. S.; Barton, J. L.; Noble, R. D.; Gin, D. L. Glycerol-Based Bicontinuous Cubic Lyotropic Liquid Crystal Monomer System for the Fabrication of Thin-Film Membranes with Uniform Nanopores. *Chem. Mater.* **2012**, *24*, 4005–4007.
- (16) Feng, X.; Tousley, M. E.; Cowan, M. G.; Wiesnauer, B. R.; Nejati, S.; Choo, Y.; Noble, R. D.; Elimelech, M.; Gin, D. L.; Osuji, C. O. Scalable Fabrication of Polymer Membranes with Vertically Aligned 1 nm Pores by Magnetic Field Directed Self-Assembly. *ACS Nano* **2014**, *8*, 11977–11986.
- (17) Matyka, M.; Khalili, A.; Koza, Z. Tortuosity-Porosity Relation in Porous Media Flow. *Phys. Rev. E* **2008**, *78*, 026306.

- (18) Zhou, M.; Nemade, P. R.; Lu, X.; Zeng, X.; Hatakeyama, E. S.; Noble, R. D.; Gin, D. L. New Type of Membrane Material for Water Desalination Based on a Cross-Linked Bicontinuous Cubic Lyotropic Liquid Crystal Assembly. *J. Am. Chem. Soc.* **2007**, *129*, 9574–9575.
- (19) Feng, X.; Nejati, S.; Cowan, M. G.; Tousley, M. E.; Wiesnauer, B. R.; Noble, R. D.; Elimelech, M.; Gin, D. L.; Osuji, C. O. Thin Polymer Films with Continuous Vertically Aligned 1 nm Pores Fabricated by Soft Confinement. *ACS Nano* **2016**, *10*, 150–158.
- (20) Dischinger, S. M.; McGrath, M. J.; Bourland, K. R.; Noble, R. D.; Gin, D. L. Effect of Post-Polymerization Anion-Exchange on the Rejection of Uncharged Aqueous Solutes in Nanoporous, Ionic, Lyotropic Liquid Crystal Polymer Membranes. *J. Membr. Sci.* **2017**, *529*, 72–79.
- (21) Resel, R.; Leising, G.; Markart, P.; Kriegbaum, M.; Smith, R.; Gin, D. Structural properties of polymerised lyotropic liquid crystals phases of 3,4,5-tris(-acryloxyalkoxy)benzoate salts. *Macromol. Chem. Phys.* **2000**, *201*, 1128–1133.
- (22) McIntosh, T. J.; Simon, S. A.; MacDonald, R. C. The Organization of N-Alkanes in Lipid Bilayers. *Biochim. Biophys. Acta, Biomembr.* **1980**, *597*, 445–463.
- (23) Govind, A. S.; Madhusudana, N. V. A Simple Molecular Theory of Smectic-C Liquid Crystals. *EPL* **2001**, *55*, 505.
- (24) Zhu, X.; Scherbina, M. A.; Bakirov, A. V.; Gorzolnik, B.; Chvalun, S. N.; Beginn, U.; Müller, M. Methacrylated Self-Organizing 2,3,4-Tris(alkoxy)benzenesulfonate: A New Concept Toward Ion-Selective Membranes. *Chem. Mater.* **2006**, *18*, 4667–4673.
- (25) Chaikin, P.; Lubensky, T. *Principles of Condensed Matter Physics*, 1st ed.; Cambridge University Press: Cambridge, UK, 1995.

- (26) Wang, J.; Wolf, R. M.; Caldwell, J. W.; Kollman, P. A.; Case, D. A. Development and Testing of a General Amber Force Field. *J. Comput. Chem.* **2004**, *25*, 1157–1174.
- (27) Wang, J.; Wang, W.; Kollman, P. A.; Case, D. A. Automatic Atom Type and Bond Type Perception in Molecular Mechanical Calculations. *J. Mol. Graphics. Modell.* **2006**, *25*, 247–260.
- (28) Case, D.; Betz, R.; Botello-Smith, W.; Cerutti, D.; Cheatham, T., III; Darden, T.; Duke, R.; Giese, T.; Gohlke, H.; Goetz, A. et al. AmberTools16. 2016.
- (29) Cook, M. J.; Wilson, M. R. Development of an All-Atom Force Field for the Simulation of Liquid Crystal Molecules in Condensed Phases (LCFF). *Mol. Cryst. Liq. Cryst.* **2001**, *357*, 149–165.
- (30) Boyd, N. J.; Wilson, M. R. Optimization of the Gaff Force Field to Describe Liquid Crystal Molecules: The Path to a Dramatic Improvement in Transition Temperature Predictions. *Phys. Chem. Chem. Phys.* **2015**, *17*, 24851–24865.
- (31) Bekker, H.; Berendsen, H. J. C.; Dijkstra, E. J.; Achterop, S.; van Drunen, R.; van der Spoel, D.; Sijbers, A.; Keegstra, H.; Reitsma, B.; Renardus, M. K. R. GROMACS: A Parallel Computer for Molecular Dynamics Simulations. Physics Computing '92 ed. 1993.
- (32) Berendsen, H. J. C.; van der Spoel, D.; van Drunen, R. GROMACS: A Message-Passing Parallel Molecular Dynamics Implementation. *Comput. Phys. Commun.* **1995**, *91*, 43–56.
- (33) Van Der Spoel, D.; Lindahl, E.; Hess, B.; Groenhof, G.; Mark, A. E.; Berendsen, H. J. C. GROMACS: Fast, Flexible, and Free. *J. Comput. Chem.* **2005**, *26*, 1701–1718.
- (34) Hess, B.; Kutzner, C.; van der Spoel, D.; Lindahl, E. GROMACS 4: Algorithms for

- Highly Efficient, Load-Balanced, and Scalable Molecular Simulation. *J. Chem. Theory Comput.* **2008**, *4*, 435–447.
- (35) Mondal, J.; Mahanthappa, M.; Yethiraj, A. Self-Assembly of Gemini Surfactants: A Computer Simulation Study. *J. Phys. Chem. B* **2013**, *117*, 4254–4262.
- (36) Martnez, L.; Andrade, R.; Birgin, E. G.; Martnez, J. M. Packmol: A Package for Building Initial Configurations for Molecular Dynamics Simulations. *J. Comput. Chem.* **2009**, *30*, 2157–2164.
- (37) Sinnokrot, M. O.; Valeev, E. F.; Sherrill, C. D. Estimates of the Ab Initio Limit for Interactions: The Benzene Dimer. *J. Am. Chem. Soc.* **2002**, *124*, 10887–10893.
- (38) Chodera, J. D. A Simple Method for Automated Equilibration Detection in Molecular Simulations. *J. Chem. Theory Comput.* **2016**, *12*, 1799–1805.
- (39) Kuriabova, T.; Betterton, M. D.; Glaser, M. A. Linear Aggregation and Liquid-Crystalline Order: Comparison of Monte Carlo Simulation and Analytic Theory. *J. Mater. Chem.* **2010**, *20*, 10366–10383.
- (40) Slater, J. C. Atomic Radii in Crystals. *J. Chem. Phys.* **1964**, *41*, 3199–3204.
- (41) Oliphant, T. E. Python for Scientific Computing. *Comput. Sci. Eng.* **2007**, *9*, 10–20.
- (42) Einstein, A. *Investigations on the Theory of the Brownian Movement*; Dover Publications: Dover, New York, USA, 1956.
- (43) Caleman, C.; van Maaren, P. J.; Hong, M.; Hub, J. S.; Costa, L. T.; van der Spoel, D. Force Field Benchmark of Organic Liquids: Density, Enthalpy of Vaporization, Heat Capacities, Surface Tension, Isothermal Compressibility, Volumetric Expansion Coefficient, and Dielectric Constant. *J. Chem. Theory Comput.* **2012**, *8*, 61–74.
- (44) Wang, L.-P.; McKiernan, K. A.; Gomes, J.; Beauchamp, K. A.; Head-Gordon, T.; Rice, J. E.; Swope, W. C.; Martnez, T. J.; Pande, V. S. Building a More Predictive

Protein Force Field: A Systematic and Reproducible Route to AMBER-FB15. *J. Phys. Chem. B* **2017**, *121*, 4023–4039.

- (45) Percec, V.; Imam, M. R.; Peterca, M.; Wilson, D. A.; Graf, R.; Spiess, H. W.; Balagurusamy, V. S. K.; Heiney, P. A. Self-Assembly of Dendronized Triphenylenes into Helical Pyramidal Columns and Chiral Spheres. *J. Am. Chem. Soc.* **2009**, *131*, 7662–7677.
- (46) Gearba, R. I.; Anokhin, D. V.; Bondar, A. I.; Bras, W.; Jahr, M.; Lehmann, M.; Ivanov, D. A. Homeotropic Alignment of Columnar Liquid Crystals in Open Films by Means of Surface Nanopatterning. *Adv. Mater.* **2007**, *19*, 815–820.
- (47) Young, O.; Wildes, A. R.; Manuel, P.; Ouladdiaf, B.; Khalyavin, D. D.; Balakrishnan, G.; Petrenko, O. A. Highly Frustrated Magnetism in SrHo₂O₄: Coexistence of Two Types of Short-Range Order. *Phys. Rev. B* **2013**, *88*, 024411.
- (48) Girolami, G. S. *X-ray Crystallography*; University Science Books: Herndon, VA, USA, 2016.
- (49) Harburn, G.; Taylor, C. A.; Welberry, T. R. *Atlas of Optical Transforms*; Cornell University Press: Ithaca, New York, USA, 1975.
- (50) Taylor, G. The Phase Problem. *Acta Cryst D* **2003**, *59*, 1881–1890.
- (51) Carey, F.; Giuliano, R. *Organic Chemistry*, 8th ed.; McGraw-Hill Companies, Inc.: USA, 2011.
- (52) Tauer, T. P.; Sherrill, C. D. Beyond the Benzene Dimer: An Investigation of the Additivity of Interactions. *J. Phys. Chem. A* **2005**, *109*, 10475–10478.
- (53) Dong, R. Y.; Goldfarb, D.; Moseley, M. E.; Luz, Z.; Zimmermann, H. Translational Diffusion in Discotic Mesophases Studied by the Nuclear Magnetic Resonance Pulsed Field Gradient Method. *J. Phys. Chem.* **1984**, *88*, 3148–3152.

- (54) Dvinskikh, S. V.; Fur, I.; Zimmermann, H.; Maliniak, A. Molecular Self-Diffusion in a Columnar Liquid Crystalline Phase Determined by Deuterium NMR. *Phys. Rev. E* **2002**, *65*, 050702.
- (55) Liu, Y.; Zhu, F. Collective Diffusion Model for Ion Conduction Through Microscopic Channels. *Biophys. J.* **2013**, *104*, 368–376.
- (56) Bruce, C. D.; Berkowitz, M. L.; Perera, L.; Forbes, M. D. E. Molecular Dynamics Simulation of Sodium Dodecyl Sulfate Micelle in Water: Micellar Structural Characteristics and Counterion Distribution. *J. Phys. Chem. B* **2002**, *106*, 3788–3793.
- (57) Shi, Y.; Xia, Z.; Zhang, J.; Best, R.; Wu, C.; Ponder, J. W.; Ren, P. Polarizable Atomic Multipole-Based AMOEBA Force Field for Proteins. *J. Chem. Theory Comput.* **2013**, *9*, 4046–4063.
- (58) Kaminski, G. A.; Stern, H. A.; Berne, B. J.; Friesner, R. A. Development of an Accurate and Robust Polarizable Molecular Mechanics Force Field from ab Initio Quantum Chemistry. *J. Phys. Chem. A* **2004**, *108*, 621–627.
- (59) Lopes, P. E. M.; Lamoureux, G.; Roux, B.; MacKerell, A. D. Polarizable Empirical Force Field for Aromatic Compounds Based on the Classical Drude Oscillator. *J. Phys. Chem. B* **2007**, *111*, 2873–2885.

TOC Graphic

